Meteoritics & Planetary Science 42, Nr 7/8, 1221–1240 (2007)
Abstract available online at http://meteoritics.org

Al-Mg isotopic evidence for episodic alteration of Ca-Al-rich inclusions from Allende

T. J. FAGAN[1†*], Y. GUAN[2††], and G. J. MACPHERSON[3]

[1]Department of Earth Sciences, Waseda University, 1-6-1 Nishiwaseda, Shinjuku, Tokyo 169-8050, Japan
[2]Laboratory for Space Sciences and Physics Department, Washington University, Saint Louis, Missouri 63130, USA
[†]Formerly of the Smithsonian Institution
[††]Present address: Division of Geological and Planetary Sciences, MC 170-25,
California Institution of Technology, Pasadena, California 91125, USA
[*]Corresponding author. E-mail: fagan@waseda.jp

(Received 13 October 2006; revision accepted 22 April 2007)

Abstract–Textures, mineral assemblages, and Al-Mg isotope systematics indicate a protracted, episodic secondary mineralization history for Allende Ca-Al-rich inclusions (CAIs). Detailed observations from one type B1 CAI, one B2, one compact type A (CTA), and one fluffy type A (FTA) indicate that these diverse types of CAIs are characterized by two distinct textural and mineralogic types of secondary mineralization: (1) grossular-rich domains, concentrated along melilite grain boundaries in CAI interiors, and (2) feldspathoid-bearing domains, confined mostly to CAI margins just interior to the Wark-Lovering rim sequence.

The Al-Mg isotopic compositions of most secondary minerals in the type B1 CAI, and some secondary minerals in the other CAIs, show no resolvable excesses of ^{26}Mg, whereas the primary CAI phases mostly yield correlated excesses of ^{26}Mg with increasing Al/Mg corresponding to "canonical" initial $^{26}Al/^{27}Al \sim 4.5–5 \times 10^{-5}$. These secondary minerals formed at least 3 Ma after the primary CAI minerals. All but two analyses of secondary minerals from the fluffy type-A CAI define a correlated increase in $^{26}Mg/^{24}Mg$ with increasing Al/Mg, yielding $(^{26}Al/^{27}Al)_0 = (4.9 \pm 2.8) \times 10^{-6}$. The secondary minerals in this CAI formed 1.8–3.2 Ma after the primary CAI minerals. In both cases, the timing of secondary alteration is consistent with, but does not necessarily require, alteration in an asteroidal setting. One grossular from the type B2 CAI, and several grossular and secondary feldspar analyses from the compact type A CAI, have excesses of ^{26}Mg consistent with initial $^{26}Al/^{27}Al \sim 4.5 \times 10^{-5}$. Especially in the compact type A CAI, where $^{26}Mg/^{24}Mg$ in grossular correlates with increasing Al/Mg, these ^{26}Mg excesses are almost certainly due to in situ decay of ^{26}Al. They indicate a nebular setting for formation of the grossular.

The preservation of these diverse isotopic patterns indicates that heating on the Allende parent body was not pervasive enough to reset isotopic systematics of fine-grained secondary minerals. Secondary mineralization clearly was not restricted to a short time interval, and at least some alteration occurred coincident with CAI formation and melting events (chondrule formation) in the nebula. This observation supports the possibility that alteration followed by melting affected the compositional evolution of CAIs.

INTRODUCTION

Calcium-aluminum-rich inclusions (CAIs) in chondritic meteorites preserve a petrologic and isotopic record of the formation and later complex processing of the first solids in the solar nebula (MacPherson et al. 1988; MacPherson 2003; Scott and Krot 2005). Most research on CAIs has focused on "primary minerals," which are rich in refractory elements such as Ca, Al, and Ti, and are considered products of interactions between dust and gas, and processes such as melting, crystallization, evaporation, and condensation under high-temperature conditions (Grossman 1972; Stolper 1982; Wark and Lovering 1982a; Yoneda and Grossman 1995; Ebel and Grossman 2000). An array of unusual isotopic signatures has been identified in CAI primary minerals. Of particular interest in this study are the excesses of $^{26}Mg/^{24}Mg$ that correlate with increasing $^{27}Al/^{24}Mg$. These Al-Mg isotopic systematics are widely interpreted as a consequence of

Table 1. Main minerals identified in the four Allende CAIs.

Name	General formula	Mineral group
Primary minerals		
Anorthite	$CaAl_2Si_2O_8$	Feldspar
Diopside	$CaMgSi_2O_6$	Pyroxene
Fassaite	$Ca(Mg,Al,Ti)(Al,Si)_2O_6$	Pyroxene
Hibonite	$Ca(Al,Mg,Ti)_{12}O_{19}$	Oxide
Melilite (Ge-Åk)	$Ca_2Al_2SiO_2$-$Ca_2MgSi_2O_7$	Sorosilicate
Spinel	$MgAl_2O_4$	Oxide
Perovskite	$CaTiO_3$	Oxide
Secondary minerals		
Anorthite	$CaAl_2Si_2O_8$	Feldspar
Fe-diopside	$Ca(Fe,Mg)Si_2O_6$	Pyroxene
Fe-spinel	$(Fe,Mg)Al_2O_4$	Oxide
Grossular	$Ca_3Al_2Si_3O_{12}$	Garnet
Monticellite	$CaMgSiO_4$	Nesosilicate
Nepheline	$(K,Na)_2Al_2Si_2O_8$	Feldspathoid
Sodalite	$Na_4Al_3Si_3O_{12}Cl$	Feldspathoid
Wollastonite	$CaSiO_3$	Pyroxenoid

Note: The naturally occurring minerals are solid solutions with variations from the tabulated formulae. Gehlenite and åkermanite end-members of the melilite solid solution are shown. Anorthite occurs as both a primary and a secondary mineral.

formation of CAIs in the presence of ^{26}Al, which decays to ^{26}Mg in a short geologic time-frame ($t_{1/2}$ = 730,000 years; see Lee et al. 1976; MacPherson et al. 1995; McKeegan and Davis 2003; Kita et al. 2005; Krot et al. 2005). The magnesium isotopic system thus has potential importance as a high-resolution relative chronometer.

In addition to their early-stage "primary" minerals, many CAIs show textural evidence for at least one episode of alteration that produced "secondary" minerals under different physical conditions at later stages of petrogenesis (Grossman and Granapathy 1975; Christophe Michel-Levy 1986; MacPherson 2003; MacPherson et al. 2005). Some of the secondary minerals (grossular, monticellite, anorthite) are formed of the same components (CaO-MgO-Al_2O_3-SiO_2-TiO_2) as the more refractory primary minerals, whereas other secondary minerals (Fe-bearing spinel, nepheline, sodalite) require an influx of relatively volatile elements (Fe, Na, Cl, Zn) (Table 1) (Hutcheon and Newton 1981; Wark 1981; Krot et al. 1995).

Mineral stabilities indicate that alteration occurred at lower temperatures than primary crystallization of the CAIs, but the setting of alteration remains a contentious issue (see summaries in Brearley 2003; MacPherson et al. 2005): some workers advocate low-temperature gas-solid reactions in the nebula (Hashimoto and Grossman 1987; Davis et al. 1994), and others advocate solid-fluid reactions on the Allende parent body (Krot et al. 1995; 1998). Determining the setting of alteration is a first-order problem regarding early solar system history and is essential for petrologic interpretation of the secondary minerals. Furthermore, if alteration occurred at an early stage in the nebula, episodic heating and cooling events might have affected compositional evolution of CAIs (MacPherson and Davis 1993; Beckett et al. 2000; MacPherson and Huss 2005; Simon et al. 2005).

The goal of this paper is to evaluate the setting of alteration by comparing the Al-Mg isotopic systematics of secondary and primary minerals in CAIs from the CV3 chondrite Allende. A nebular setting of alteration requires a relatively short duration of time between primary and secondary minerals, whereas a parent-body setting requires a longer interval. The quantitative distinction between "short" and "long" depends on estimates of the lifetime of CAI-sized nodules in the solar nebula and time scales of asteroidal accretion. These are not straightforward issues, as turbulence and outward flows of gas may counter the inward trajectory of small particles due to gas drag, and accretion of asteroid-sized bodies can be affected by a variety of parameters (e.g., Shu et al. 1996; Cuzzi and Zahnle 2004; Cuzzi et al. 2005). Nonetheless, the time scale of ^{26}Al decay is appropriate for establishing a chronology of alteration over a critical duration of 2 to 3 million years after formation of the primary CAI phases. Primary minerals in many CAIs closed to Al-Mg isotopes with initial $^{26}Al/^{27}Al$ ratios near 5×10^{-5}. This initial ratio has been termed "canonical" because of its widespread occurrence (MacPherson et al. 1995); whether the canonical value truly represents first-generation crystallization of CAIs or a subsequent resetting event(s) has been questioned by recent work (Young et al. 2005; Cosarinsky et al. 2006). We do not address this issue in this study, but rather use the canonical ratio (here we use 4.5×10^{-5}) as a benchmark value with which to compare the relative formation times of primary versus secondary phases in CAIs. We explicitly accept the interpretation that ^{26}Mg excesses correlated with Al/Mg in CAIs reflect the in situ decay of ^{26}Al within a relatively homogeneous isotopic reservoir, with the consequence that subsequent decay of ^{26}Al can be used as a chronometer (McKeegan and Davis 2003). In this project, we focus on types A and B CAIs from Allende, whose primary phases are characterized by canonical initial ratios of $^{26}Al/^{27}Al$ and which contain well-developed assemblages of texturally distinct secondary minerals (for background on the CAI nomenclature used herein, such as "type A" and "type B," see Grossman 1975; Wark and Lovering 1982b; MacPherson and Grossman 1984; summaries can be found in reviews by Grossman 1980, MacPherson et al. 1988, and MacPherson 2003).

ANALYTICAL METHODS

Petrography and Mineral Compositions

An initial set of fifteen Allende CAIs (4 type B1, 6 fluffy type A, 4 B2 and 1 compact type A) from the Smithsonian Institution (SI) collection were characterized using a petrographic microscope and a JEOL JSM-840A scanning

electron microscope (SEM) with backscattered electron (BSE) and energy dispersive X-ray (EDS) detectors, in the Smithsonian's Department of Mineral Sciences. Four representative CAIs were selected from the initial set for more detailed characterization using the same instruments plus a cathodoluminescence microscope and a JEOL 8900 electron microprobe outfitted with five wavelength dispersive detectors (WDS). Quantitative major-element compositions of minerals in the CAIs were determined by EDS and WDS. EDS analyses were collected by G. L. Kim using a 15 kV focused beam (~1 μm). Some WDS analyses and images were collected using a JEOL JXA-8900 electron microprobe with four WDS detectors at Waseda University. All elemental analyses were collected using well-characterized silicate and oxide standards. The WDS analyses were collected using 15 kV voltage, spot sizes of 1 or 2 μm, and currents ranging from 10 to 20 nA. The small grain sizes of the nepheline and sodalite in the CAIs necessitated small focused beam spots, so alkalis were analyzed first during WDS in order to minimize the effects of alkali volatilization. X-ray elemental maps covering a variety of scales were collected by both EDS and WDS.

Ion Microprobe Analyses

In situ magnesium isotopic measurements were carried out with the Cameca IMS 6f ion microprobe at Arizona State University, using procedures similar to those describe in Fahey et al. (1987; also see MacPherson et al. 2003). A −12.5 kV O^- primary beam of 0.05–0.2 nA was focused to a ≤5 μm diameter spot for all the measurements. The sample voltage was set to +10 kV and secondary ions were collected with an energy band-pass of ~50 eV, an imaged field of ~75 μm, and a mass-resolving power of ~3500. The masses measured were ^{24}Mg, ^{25}Mg, ^{26}Mg, and ^{27}Al. Excesses of ^{26}Mg ($\equiv ^{26}Mg^*$), corrected for both instrumental and intrinsic mass fractionations, were calculated using a linear law; given our analytical uncertainties, possible errors in determining radiogenic $^{26}Mg^*$ due to use of the linear law correction are insignificant especially at relatively high Al/Mg. The Al/Mg sensitivity factors were determined using terrestrial standards including spinel, melilite, and plagioclase. Standards matching several secondary minerals were not available. However, noting that the sensitivity factors for the two silicate standards are within ~10% of each other (also see Stoll and Jochum 1999), we corrected the $^{27}Al/^{24}Mg$ values for all of the secondary minerals using the plagioclase sensitivity factor and assigned an error of 10%. The program Isoplot v. 3.0 (Ludwig 2003) was used for regressions of isotopic data. Isoplot calculates a "probability of fit" parameter, which is a measure of the likelihood that the observed scatter of data points away from a straight line fit is due entirely to analytical uncertainty. As a guideline, Ludwig suggests that a York (1969) regression is justified if the probability of fit exceeds 0.15.

RESULTS

Textures and Mineralogy

As discussed by MacPherson (2003), the terms "primary" and "secondary" are useful, yet potentially confusing. In this study, we classify minerals as "secondary" if textures unambiguously indicate that they formed by partial replacement of a pre-existing solid phase. In general, secondary minerals occur as relatively small crystals along fractures or serrated crystal margins of pre-existing minerals. Secondary minerals may have significant concentrations of FeO, Na_2O, K_2O, or Cl, whereas primary minerals are dominated by the more refractory components CaO-Al_2O_3-TiO_2-MgO-SiO_2 (Table 1).

The reader is cautioned about one potential source of confusion in the following sections, concerning the mineral anorthite. Anorthite occurs in two very different forms: as large, primary crystals in type B CAIs that clearly crystallized from a melt, and as tiny secondary crystals in types A and B CAIs that are secondary replacements after melilite. Some type B CAIs can have both, and in the descriptions and discussions that follow we endeavor to make clear which variety of anorthite we are referring to.

Primary Textures and Minerals

The four CAIs investigated in detail in this study include one type B1 (CAI 3655A), one type B2 (4022-1), one compact type A (3898), and one fluffy type A (3529-47) (Figs. 1 and 2).

Our thin section of 3655A (Figs. 1a and 2a) is a wedge-shaped slice from an originally >1 cm sized spheroidal type B1 CAI, with a polymineralic core, a melilite-rich mantle, and a Wark-Lovering rim sequence (Wark and Lovering 1977) consisting mainly of a continuous layer of diopside. The primary minerals in the core are coarse-grained fassaite, anorthite, melilite and Mg-spinel, whereas the CAI mantle is dominated by melilite and spinel. Spinel and hibonite crystals, commonly with tiny perovskite inclusions, occur inboard of the rim sequence. The mineralogy and textures of CAI 3655A have been described in previous studies that focused on zoning in fassaite (Paque 1990), major-element composition (Wark and Lovering 1982b), and Al-Mg isotope systematics and trace-element compositions of primary phases (Kennedy et al. 1997). These studies show that CAI 3655A formed during multi-stage igneous evolution; primary minerals have heavy mass-dependent Mg-isotopic enrichments suggestive of melt evaporation, and primary anorthite has radiogenic ^{26}Mg excesses arising from in situ decay of ^{26}Al at an initial abundance $^{26}Al/^{27}Al \sim 4 \times 10^{-5}$.

CAI 4022 is a type B2 CAI, ~0.8 cm in diameter, with a slight enrichment of melilite near the margin (Figs. 1b and 2b), but nothing like the massive melilite mantle such as seen in 3655A. Melilite occurs as elongate tabular crystals up to

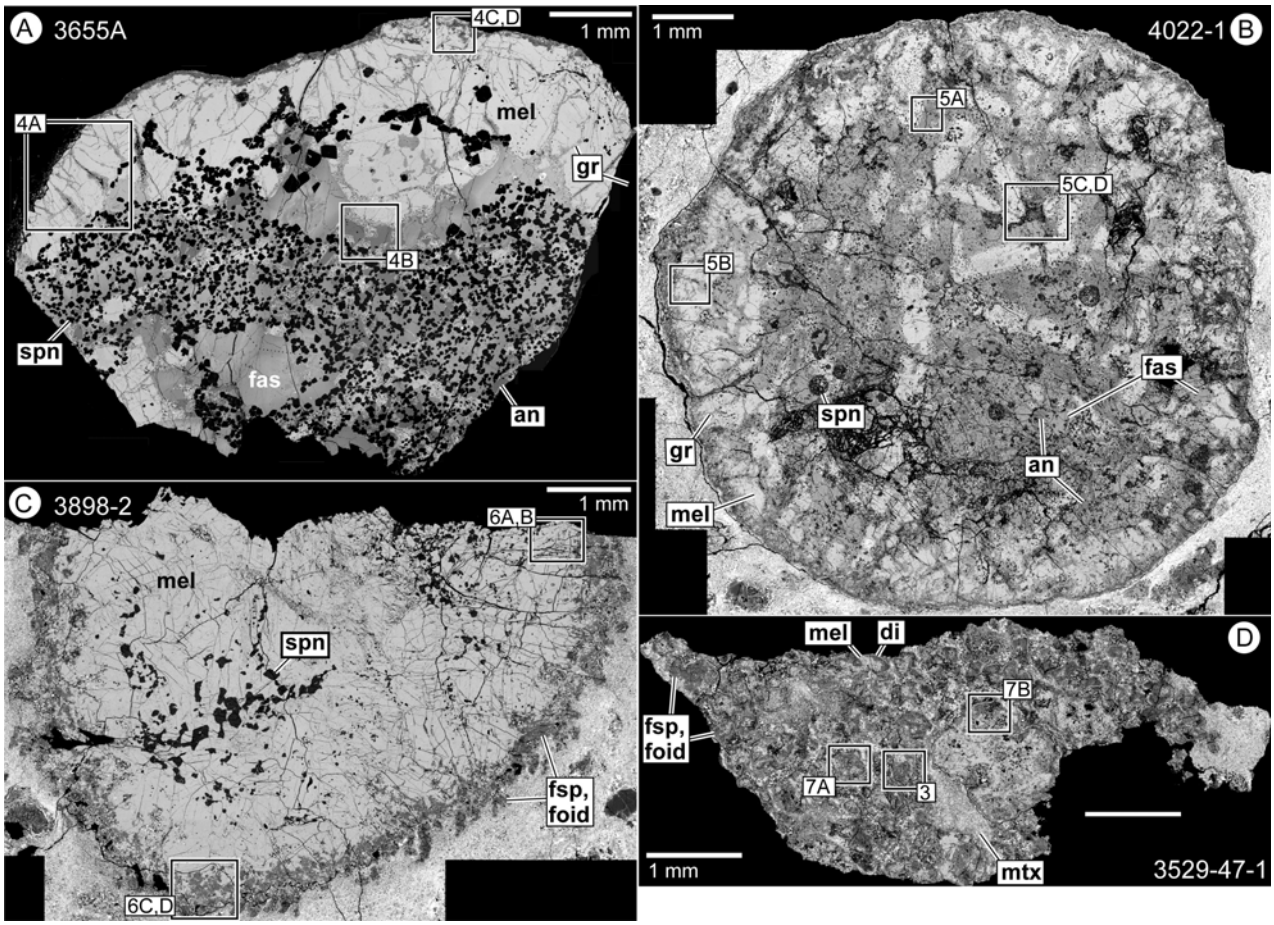

Fig. 1. Backscattered electron (BSE) mosaics of (a) type B1 CAI 3655A, (b) type B2 CAI 4022-1, (c) compact type A CAI 3898-2, and (d) fluffy type A CAI 3529-47-1. Compare these figures with false-color elemental maps in Fig. 2. Mineral abbreviations here and in subsequent images: an = primary anorthite; di = diopside; fas = fassaite; Fe-sp = Fe-bearing spinel; foid = feldspathoid; fsp = secondary feldspar; gr = grossular; mel = melilite; mon = monticellite; mtx = internodule matrix; ne = nepheline; pv = perovskite; sod = sodalite; spn = spinel; wo = wollastonite.

1 mm in length, whereas fassaite and primary anorthite crystals are generally ≤0.5 mm across. Primary spinel occurs as dispersed individual crystals that are included within other primary phases, in elongate palisades (Wark and Lovering 1982a), and in spherical clusters ("framboids"). An outermost layer of diopside on the Wark-Lovering rim marks the outer boundary of the CAI.

CAI 3898 is a spheroidal compact type A (about 50% is preserved in our thin section) (Figs. 1c and 2c), and has been described in previous studies that addressed its $^{87}Sr/^{86}Sr$ isotopic composition (Gray et al 1973; Podosek et al. 1991). The interior of the CAI is dominated by coarse-grained tightly interlocking crystals of melilite with inclusions of spinel plus minor fassaite and rhönite. Melilite crystals in the inner portion of the CAI are generally more åkermanitic than melilite near the CAI margin. As noted previously (Podosek et al. 1991), individual melilite crystals are reversely zoned, with cores that are more magnesium-rich than the rims, suggesting that this CAI did not form by simple fractional crystallization of a liquid. A thin rim of fine-grained diopside forms the outermost layer of the convoluted CAI margin. Hibonite, spinel and perovskite also occur as tiny grains near the diopside rim. Podosek et al. (1991) also reported detailed ion microprobe analyses of Al-Mg isotopes in primary melilite, hibonite, fassaite and spinel. Their data indicated that the CAI formed with initial $^{26}Al/^{27}Al \sim 4.5 \times 10^{-5}$.

CAI 3529-47-1 is a fluffy type A CAI consisting of numerous melilite-rich nodules separated by fine-grained meteorite matrix (Figs. 1d and 2d). Within the nodule interiors, gehlenite-rich melilite crystals host abundant inclusions of Mg-spinel and fine-grained perovskite. Each melilite-rich nodule is surrounded by a spinel- and perovskite-rich margin overlain by a ~10 μm thick pyroxene rim. The pyroxene grades in composition progressively outwards from Ti- and Al-rich fassaite in contact with the underlying spinel toward near-end-member diopside in the outermost rim. Some nodule edges appear to be broken surfaces lacking a rim sequence. No reaction textures between minerals from the nodule interiors and inter-nodule matrix grains were noted at these boundaries (Fig. 3).

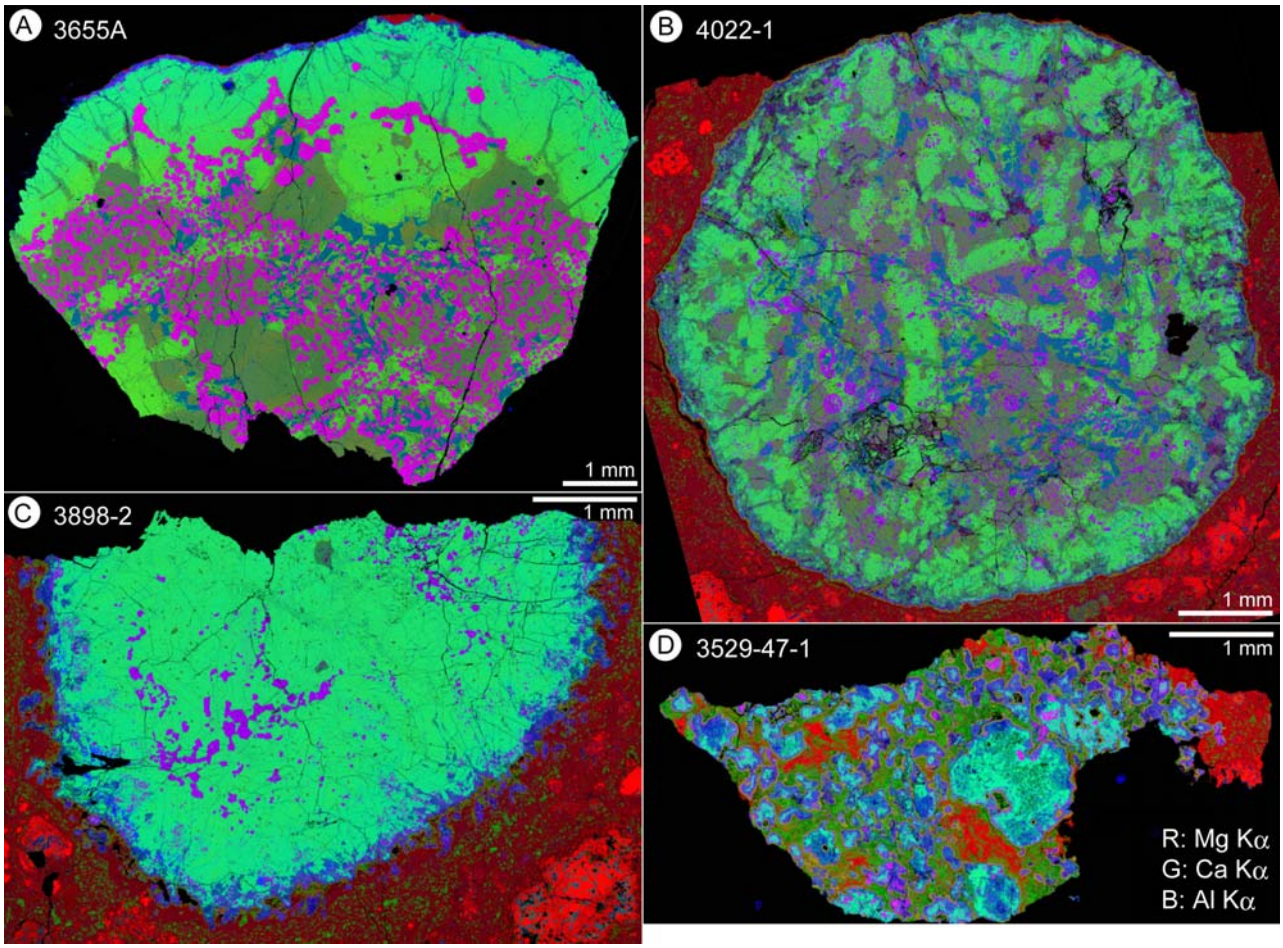

Fig. 2. False-color elemental maps of four CAIs from Allende: red = Mg K; green = Ca K; blue = Al K.

Secondary Textures and Minerals

Two texturally distinct settings for alteration mineral assemblages were recognized in each of the four CAIs: (1) grossular-rich veins and relatively equant domains that we will refer to as "patches," and (2) secondary anorthite + feldspathoid-bearing domains. Both types of alteration assemblages are commonly in contact with melilite and likely formed by replacement of that phase. The grossular-rich veins and patches occur mainly in the CAI interiors, whereas the secondary anorthite + feldspathoid alteration occurs mostly (but not exclusively) in a semi-continuous rim just inboard of the Wark-Lovering rim sequences around the CAIs. Electron microprobe analyses of the grossular typically yield stoichiometric garnet formulae with minor substitution of Mg and Fe for Ca (Table 2). Much of the secondary anorthite has a lath-like texture (Fig. 3) and shows small, but consistent deviations from feldspar stoichiometry, with enrichments in Al, Fe, and Mg that may be a result of beam overlap onto very fine-grained spinel or pyroxene (Table 2). Less porous, more tabular secondary anorthite was identified in CAIs 4022-1 and 3898-2; this feldspar shows blue to white cathodoluminescence and is stoichiometric (Table 2). Electron microprobe analyses of nepheline and sodalite are deficient in alkalis relative to stoichiometric feldspathoids, and which almost certainly reflect volatile loss during electron beam bombardment. In contrast, the Al and Si are close to stoichiometric for both sodalite and nepheline (Table 2).

Although both types of secondary assemblage were identified in each of the four CAIs investigated in this study, the specific textures, mineral assemblages and relative abundances of grossular-rich versus feldspar + feldspathoid-bearing domains vary among these CAIs and are described separately.

CAI 3655A (B1): The grossular-rich alteration domains in this CAI occur as equant patches in the CAI core and as veins along melilite grain boundaries in the CAI mantle. The grossular occurs as equant, anhedral grains less than 15 μm in diameter (Figs. 4a and 4b), and is intricately intergrown with fine-grained monticellite. Melilite immediately adjacent to the grossular-rich alteration domains contains abundant vacant pores. Wollastonite occurs with grossular and monticellite in alteration patches in the core of the CAI, but

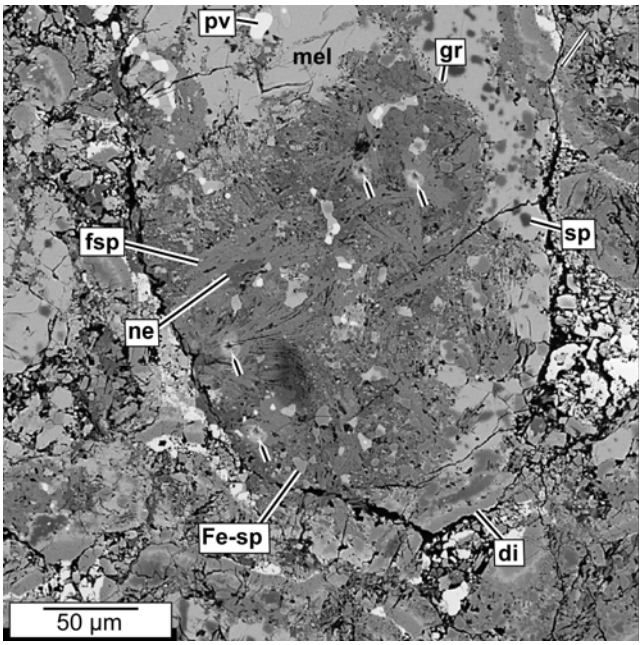

Fig. 3. BSE image of fluffy type A nodule with broken surfaces in contact with internodule matrix. BSE image is overlain on an SE image with throughput adjusted so that compositional contrasts are shown in BSE and pits excavated during SIMS analyses are highlighted by SE. Craters sputtered during SIMS analyses are denoted by arrows; mineral abbreviations as in Fig. 1.

was not found in veins in the CAI mantle. The grossular-rich veins appear to have formed by pseudomorphic replacement of melilite along grain boundaries, cleavage traces, and cracks in melilite. Although the alteration patches in the core primarily replace melilite, serrated margins along neighboring primary anorthite grain boundaries suggest that some anorthite also might have decomposed during alteration (Fig. 4b).

Most of the secondary feldspar + feldspathoid-bearing alteration in 3655A is concentrated in an outer zone between the Wark-Lovering rim and the mantle melilite (Figs. 4c and 4d). The alteration patches and the rim domains are characterized by a consistent mineral sequence, with grossular occurring directly in contact with melilite, secondary anorthite mantling the grossular, and nepheline or sodalite exterior to the anorthite (Fig. 4d). Spinel in the alteration patches is generally Fe-bearing and commonly contains detectable Zn as well; secondary diopside is rare. Grossular crystals may occur in the interior of rim alteration patches as well as along the fringe. As elsewhere, the secondary feldspar in these regions has an elongate lath-like shape (Fig. 4d).

CAI 4022-1 (B2): Grossular-bearing veins in CAI 4022-1 are similar to those observed in 3655A in that they are dominated by fine-grained (generally <5 μm) intergrown grossular and monticellite, they occur throughout the CAI, and they commonly transect melilite crystals or occur along melilite crystal boundaries (Figs. 5a and 5b). Anorthite occurs instead of monticellite in some veins near the CAI margin. Secondary anorthite exhibits both lath-like and slightly coarser, more equant textures (Fig. 5b). Unlike the veins in 3655A, several grossular-rich veins in 4022-1 occur within primary anorthite crystals, apparently replacing the anorthite.

Secondary feldspar + feldspathoid-bearing alteration patches occur in the interior of CAI 4022-1 and they are in contact with all of the major primary minerals (Figs. 5c and 5d). Sodalite and nepheline in the interior of the alteration patches are for the most part separated from primary minerals by a discontinuous fringe of grossular. Similar to the feldspathoid-rich domains in CAIs 3655A, the feldspathoid alteration patches in the interior of 4022-1 include secondary anorthite; however, the anorthite does not occur as elongate laths, but forms coarser-grained, more equant, tabular crystals (Fig. 5d). Furthermore, this secondary anorthite does not form a concentric layer separating feldspathoids from the grossular fringe. Feldspathoids in the alteration patches are intergrown with elongate, fine (<1 μm across) stringers of Fe-bearing spinel, and somewhat coarser (~5 μm across) equant crystals of high-Ca pyroxene with variable Mg/(Mg + Fe).

Feldspathoids also occur in the thin layer of alteration minerals just interior to the Wark-Lovering rim that forms the outer margin of CAI 4022. Similar to the feldspathoid-rich zone in CAI 3655A, a thin discontinuous fringe of fine-grained grossular occurs along the inner boundary of the alteration layer. The layer is characterized by fine-grained feldspathoids intergrown with laths of secondary feldspar and stringers of Fe-bearing spinel. Electron microprobe analyses of these phases rarely yield stoichiometric results, owing to the fine-grained and intergrown nature of the minerals.

CAI 3898 (Compact Type A): Secondary minerals in CAI 3898 are restricted mostly to the CAI margin, just interior to the Wark-Lovering rim sequence (Figs. 1c and 2c). Grossular-bearing veins occur in CAI 3898, but are much less abundant than in the type B CAIs, and are not found in the inner core of the CAI. Also, whereas the alteration veins in the type B CAIs contain abundant monticellite in addition to grossular, the veins in 3898 consist almost entirely of grossular, with occasional secondary anorthite or feldspathoid (Figs. 6a and 6b). Monticellite and wollastonite were not identified in CAI 3898.

The secondary feldspar + feldspathoid assemblage occurs both in the wide continuous zone inboard of the Wark-Lovering diopside rim and in isolated patches enclosed by melilite near the CAI margin. Secondary minerals near the rim of 3898 exhibit essentially the same textural occurrence as observed in CAI 3655A: melilite is mantled by a discontinuous fringe of grossular; grossular is in contact with secondary lath-like anorthite, and nepheline and sodalite occur in the central portions of these alteration domains; some

Table 2. Representative electron microprobe analyses (wt%).

CAI	3655A				4022-1						3898-2
Mineral	Primary anorthite	Sec. feldspar	Grossular	Sodalite	Primary anorthite	Lath sec. feldspar	Grossular	Grossular	Tab. sec. feldspar	Sodalite	Grossular
SiO_2	42.7	38.1	39.3	37.2	43.1	37.6	40.6	39.4	43.3	39.2	39.7
TiO_2	<0.07	0.11	0.15	<0.07	0.098	0.128	<0.07	<0.07	<0.07	<0.07	<0.07
Al_2O_3	37.0	38.6	21.8	33.6	35.6	36.5	21.9	23.3	36.8	31.4	21.6
Cr_2O_3	<0.085	<0.085	<0.085	<0.085	<0.085	<0.085	<0.085	<0.085	<0.085	<0.085	<0.085
FeO	<0.10	1.42	<0.10	<0.10	<0.10	0.894	<0.10	0.423	<0.10	0.19	1.62
MgO	0.13	1.51	0.75	<0.04	0.203	3.484	1.134	0.645	<.04	1.02	0.31
CaO	19.8	17.8	36.3	0.26	20.6	16.2	37.9	37.4	20.8	1.96	36.9
Na_2O	<0.11	0.18	n.a.	23.6	0.15	0.899	<0.11	<0.11	<0.11	17.8	<0.11
K_2O	<0.03	<0.03	n.a.	<0.03	<0.03	<0.03	<0.03	<0.03	<0.03	0.10	<0.03
Cl	n.a.	<0.01	n.a.	5.52	<0.01	0.069	<0.01	<0.01	<0.01	6.87	<0.01
Total[a]	99.8	97.8	98.5	99.0	99.7	95.8	101.7	101.3	101.0	97.1	100.3
	Structural formulae										
Oxygen	8	8	8	12	8	8	12	12	8	12	12
Si	1.98	2.00	1.82	2.84	2.01	1.83	3.00	2.93	1.99	3.03	3.00
Al	2.02	1.99	2.18	3.03	1.95	2.10	1.91	2.04	1.99	2.87	1.91
Ti	b.d.	0.003	0.004	b.d.	0.003	0.005	b.d.	b.d.	b.d.	b.d.	b.d.
Cr	b.d.	b.d.	b.d.	b.d.	b.d.	b.d.	b.d.	b.d.	b.d.	b.d.	b.d.
Fe	b.d.	b.d.	0.057	b.d.	b.d.	0.036	b.d.	0.026	b.d.	0.012	b.d.
Mg	0.009	0.016	0.108	b.d.	0.014	0.253	0.125	0.071	b.d.	0.117	0.125
Ca	0.984	0.993	0.913	0.020	1.03	0.844	3.00	2.97	1.02	0.162	3.00
Na	b.d.	0.012	0.016	3.49	0.014	0.085	b.d.	b.d.	b.d.	2.67	b.d.
K	b.d.	b.d.	b.d.	b.d.	b.d.	b.d.	b.d.	b.d.	b.d.	0.009	b.d.
Cl	n.a.	n.a.	b.d.	0.714	b.d.	0.007	b.d.	b.d.	b.d.	0.901	b.d.
Total	5.00	5.01	5.09	10.1	5.02	5.16	8.04	8.04	5.01	9.77	8.04

Table 2. *Continued.* Representative electron microprobe analyses (wt%).

CAI	3898-2				3529-47-1						
Mineral	Nepheline	Tab. sec. feldspar	Melilite	Lath sec. feldspar	Grossular	Nepheline	Sodalite	Melilite	Lath sec. feldspar	Lath sec. feldspar	Melilite
SiO_2	41.6	43.3	24.3	39.0	39.7	43.5	38.9	22.5	42.3	39.3	32.3
TiO_2	<0.07	<0.07	<0.07	0.12	<0.07	0.13	<0.07	<0.07	<0.07	0.08	<0.07
Al_2O_3	35.8	35.2	33.6	39.6	21.6	37.3	31.8	34.3	36.1	39.8	19.8
Cr_2O_3	<0.085	0.09	<0.085	<0.085	<0.085	<0.085	<0.085	<0.085	<0.085	<0.085	<0.085
FeO	0.15	<0.10	<0.10	1.00	1.62	0.77	<0.10	<0.10	0.25	0.38	<0.10
MgO	0.57	0.10	1.28	1.32	0.31	0.76	<.04	0.77	0.05	0.48	6.69
CaO	4.45	18.9	39.3	18.1	36.9	3.24	0.16	41.9	20.5	19.2	41.9
Na_2O	14.70	0.26	<0.11	0.20	<0.11	13.4	18.9	<0.11	0.11	0.29	<0.11
K_2O	1.69	<0.03	<0.03	0.03	<0.03	1.58	<0.03	<0.03	<0.03	<0.03	<0.03
Cl	<0.01	<0.01	<0.01	<0.01	<0.01	<0.01	7.81	0.02	<0.01	0.02	<0.01
Total[a]	99.1	98.1	98.7	99.5	100.3	100.8	95.9	99.6	99.3	99.6	100.7
	Structural formulae										
Oxygen	8	8	7	8	12	8	12	7	8	8	7
Si	1.98	2.04	1.12	1.83	2.99	2.02	3.06	1.04	1.98	1.84	1.46
Al	2.02	1.96	1.82	2.19	1.92	2.04	2.95	1.86	1.99	2.20	1.06
Ti	b.d.	b.d.	b.d.	0.004	b.d.	0.004	b.d.	b.d.	b.d.	0.003	b.d.
Cr	b.d.	0.003	b.d.	b.d.	b.d.	b.d.	b.d.	b.d.	b.d.	b.d.	b.d.
Fe	0.006	b.d.	b.d.	0.039	0.103	0.030	b.d.	b.d.	0.010	0.015	b.d.
Mg	0.041	0.007	0.088	0.092	0.035	0.053	b.d.	0.053	0.003	0.033	0.452
Ca	0.228	0.956	1.94	0.907	2.98	0.161	0.013	2.07	1.03	0.964	2.03
Na	1.36	0.024	b.d.	0.018	b.d.	1.21	2.88	b.d.	0.010	0.026	b.d.
K	0.103	b.d.	b.d.	0.002	b.d.	0.094	b.d.	b.d.	b.d.	b.d.	b.d.
Cl	b.d.	b.d.	b.d.	b.d.	b.d.	b.d.	1.04	0.001	b.d.	0.001	b.d.
Total	5.74	4.99	4.96	5.08	8.04	5.61	9.53	5.02	5.02	5.08	5.00

[a]Sodalite totals adjusted for O as Cl.

b.d. = below detection. n.a. = not analyzed. MnO was not detected in analyses shown. All analyses by WDS.

Mineral abbreviations: lath/tab. sec. feldspar = secondary feldspar with lath versus tabular texture.

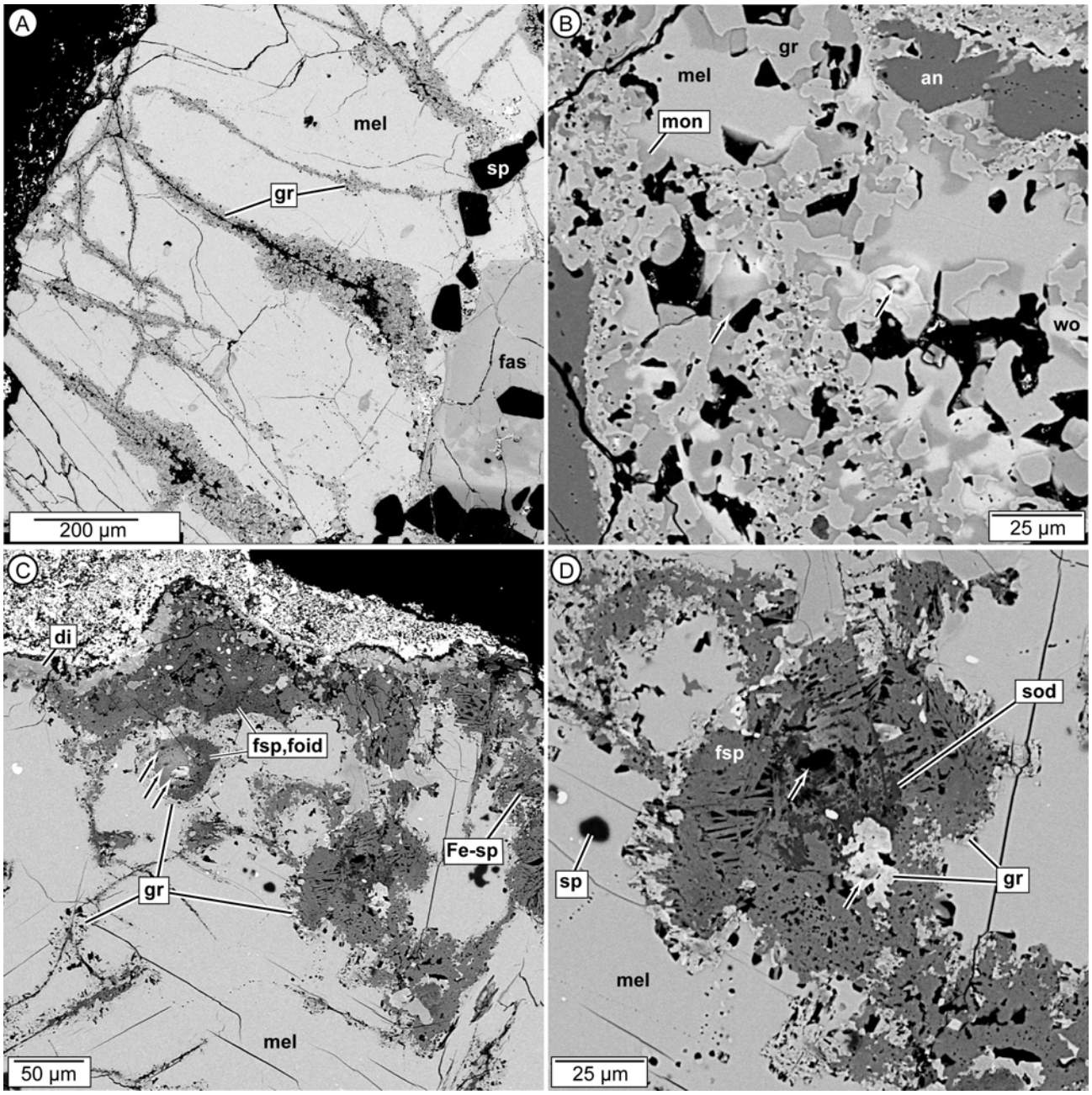

Fig. 4. BSE image (a) and BSE/SE overlays (b, c, d) of type B1 CAI 3655A. a) Grossular-rich veins in melilite-rich mantle of CAI. b) Extensively pseudomorphed melilite from core of CAI. c) Altered domains near rim of CAI. Very bright material in upper part of image consists of Allende matrix. Diopside along CAI margin is from the altered Wark-Lovering rim. Secondary minerals occur adjacent to the Wark-Lovering rim and in alteration patches enclosed by melilite near the CAI margin. d) Detailed image from (c) of feldspathoid alteration patch. Note the presence of grossular along the rim and in the center of the alteration patch, the lath-like texture of secondary feldspar and the occurrence of sodalite in the center of the patch. Craters sputtered during SIMS analyses are denoted by arrows; mineral abbreviations as in Fig. 1.

grossular crystals occur in the inner portions of alteration patches as well as along the fringing margins; Fe-bearing spinel occurs within the alteration patches (Figs. 6c and 6d). In rare cases, secondary feldspar is tabular and yields more stoichiometric electron microprobe analyses than the lath-like secondary feldspar (Table 2).

CAI 3529-47-1 (Fluffy Type A): Secondary minerals in CAI 3529-47-1 form a much greater fraction of the whole CAI than in any of the others inclusions studied, and are dominated by the feldspar + feldspathoid assemblage (Figs. 1d and 2d). Similar to compact type-A CAI 3898-2 grossular-rich veins are rare; monticellite is absent. Within each of the nodules

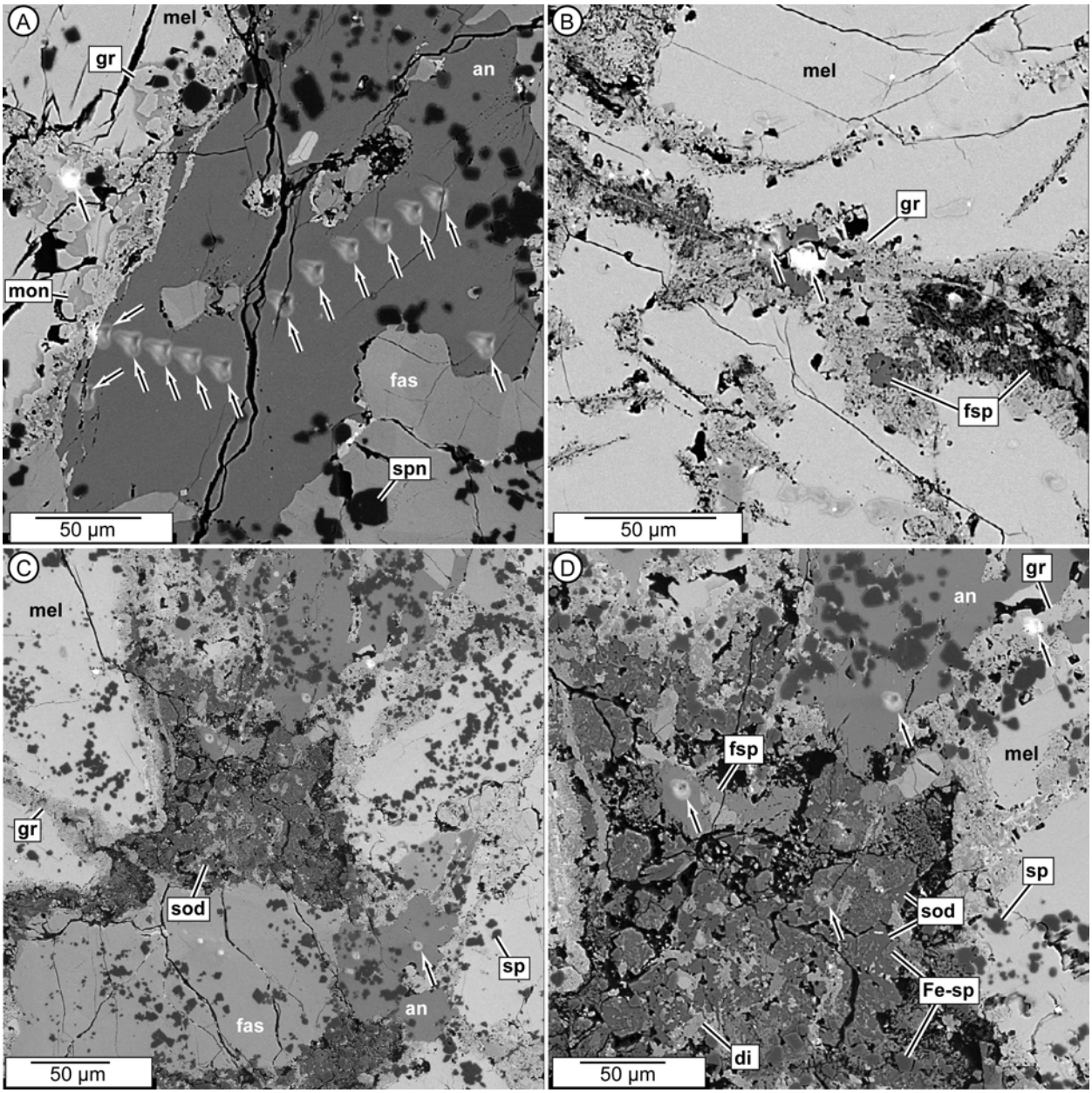

Fig. 5. BSE/SE overlay images of type B2 CAI 4022-1. Craters sputtered during SIMS analyses are denoted by arrows. a) Intersecting grossular-bearing veins in interior of CAI, and SIMS analyses in primary anorthite (center) and grossular (upper left). Arrows from lower right to upper left denote analyses considered representative of target minerals. Arrows pointing from upper right to lower left show SIMS craters on primary/secondary mineral boundaries or on mineralized cracks; these analyses were not considered in our interpretation of alteration history. b) Grossular-bearing vein with secondary anorthite near margin of CAI. Some secondary anorthite has lath-like texture; some (center) has more equant, coarse-grained form. c) Feldspathoid-bearing alteration patch, grossular-bearing veins and primary minerals in interior of CAI. d) Detailed view of alteration patch shown in (c). Note the relatively coarse grain size of secondary feldspar (here stoichiometric anorthite) and presence of diopside (with variable Fe/[Fe + Mg]) as a secondary mineral. Mineral abbreviations as in Fig. 1.

composing the CAI, secondary feldspar + feldspathoid-bearing domains occupy the irregular regions between the highly serrated melilite crystals and the Wark-Lovering rims (Figs. 7a and 7b). The melilite crystal margins are mantled by a discontinuous grossular fringe, which in turn is in contact with lath-like secondary anorthite. Grossular may occur in the interiors of altered domains as well as on the fringing margins. Nepheline and sodalite are concentrated away from the melilite. Iron-bearing spinel occurs as individual crystals generally <2 µm across and as thin strands of finer-grained crystals in contact with secondary feldspar and feldspathoids. Along broken nodule surfaces, the alteration minerals occur adjacent to inter-nodule matrix grains with no apparent reaction textures (Fig. 3).

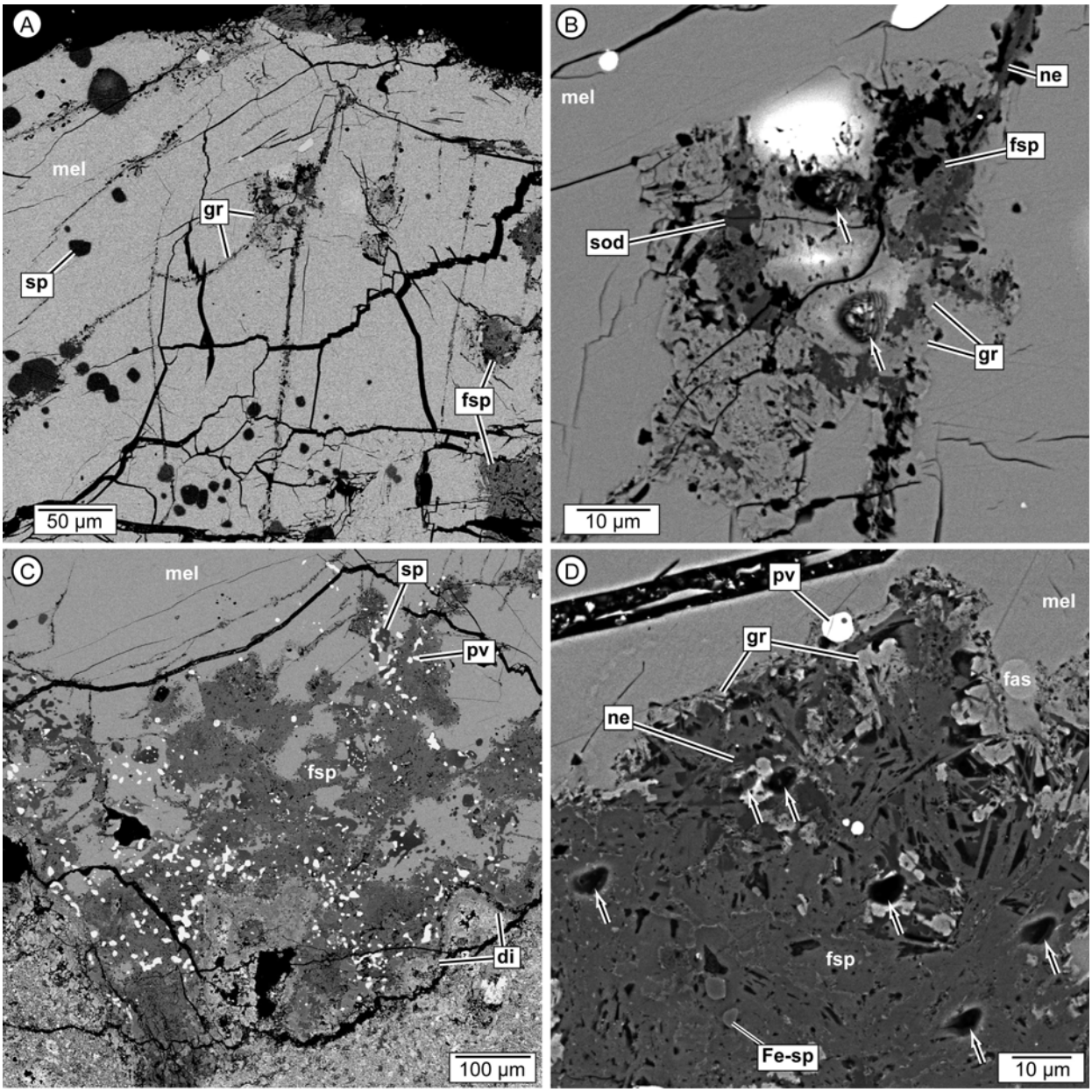

Fig. 6. BSE images of compact type A CAI 3898-2. a) Grossular-bearing veins in interior of CAI. Note the paucity of veins compared with the type B CAIs. b) Detailed image from center of (a) showing thick portion of vein and pits excavated by SIMS. c) Altered domains near rim of CAI. Bright material in lower part of image consists of Allende matrix. Diopside along CAI margin is from the altered Wark-Lovering rim. Secondary minerals occur adjacent to the Wark-Lovering rim and in alteration patches enclosed by melilite near the CAI margin. d) Detailed image from (c) showing portion of a feldspathoid alteration patch. Note grossular along the fringe and in the center of the alteration patch, the lath-like texture of secondary feldspar and the occurrence of nepheline in the interior of the patch. Craters sputtered during SIMS analyses are denoted by arrows in (b) and (d). Mineral abbreviations as in Fig. 1.

Al-Mg Isotopic Results

All isotopic data are given in Table 3 and shown graphically in Fig. 8.

Type B1 CAI 3655A

Primary anorthite from CAI 3655A shows well-defined correlated excesses of ^{26}Mg with $^{27}Al/^{24}Mg$ (Table 3; Figs. 8a and 8b); a regression of the anorthite and spinel analyses yields a line with a high probability of fit (0.88, MSWD = 0.22) and initial $^{26}Al/^{27}Al = (4.25 \pm 0.27) \times 10^{-5}$, comparable to the determination by Kennedy et al. (1997) of $[^{26}Al/^{27}Al]_0 = (3.95 \pm 0.42) \times 10^{-5}$ and within error of canonical values. Spinel has $^{26}Mg/^{24}Mg$ within error of the common value reported by Catanzaro et al. (1966; also see Young and Galy 2004). The three melilite analyses show no resolvable ^{26}Mg

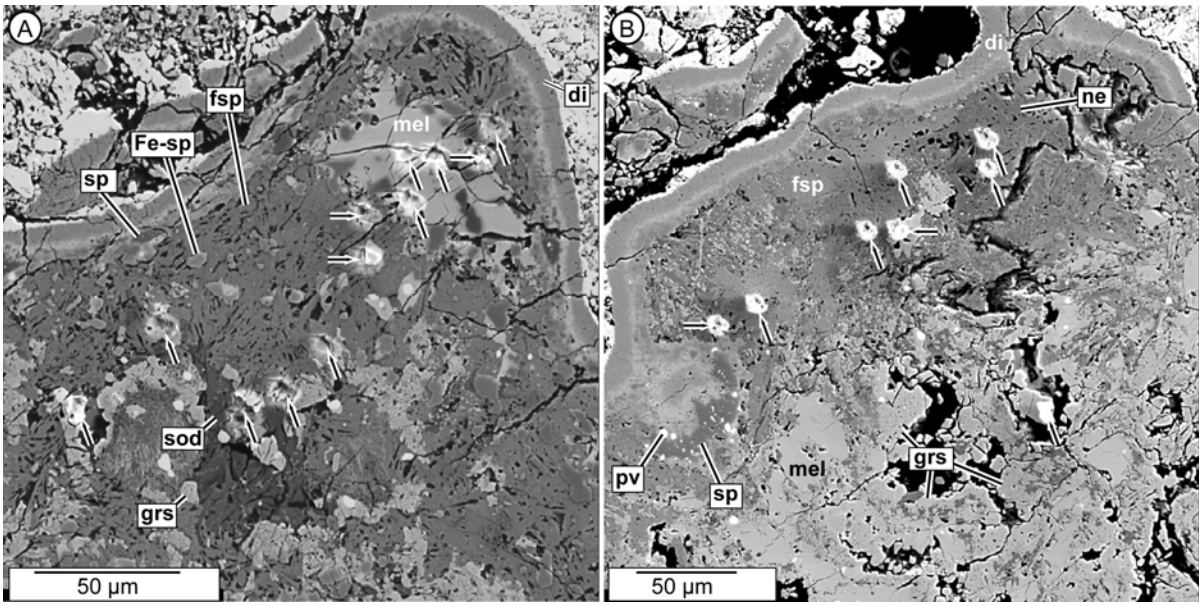

Fig. 7. BSE/SE overlay images of fluffy type A CAI 3529-47-1. a) Original melilite has been extensively replaced by secondary feldspar and feldspathoids. Note the lath-like texture of secondary feldspar, corroded crystal boundaries of melilite and discontinuous grossular fringe on melilite. b) Grossular occurs as fringe along melilite grain boundaries, as shown previously, and within interior of melilite. Craters sputtered during SIMS analyses are denoted by arrows. Arrows from lower right to upper left denote analyses considered representative of target minerals. Arrows pointing horizontally show SIMS craters on mineral boundaries; these analyses were not considered in our interpretation of alteration history. Mineral abbreviations as in Fig. 1.

excesses and two of these (at very low Al/Mg) show apparent $^{26}Mg/^{24}Mg$ deficits of uncertain origin. A weighted regression through all of the primary mineral data yields a line consistent with near-canonical initial $^{26}Al/^{27}Al$, but a low $^{24}Mg/^{26}Mg$ intercept and a poor probability of fit that are both due to the apparent $^{26}Mg/^{24}Mg$ deficits in melilite as noted above. Other recent SIMS studies also report melilite results that are difficult to interpret and suggest that melilite may be susceptible to Mg-isotopic resetting (Cosarinsky et al. 2006).

The secondary minerals in 3655A show no clear evidence for having formed in the presence of live ^{26}Al. One sodalite at $^{27}Al/^{24}Mg = 37$ (B1-1-08) shows a hint of an excess, but is nearly within 2σ of isotopically normal Mg. All other secondary minerals—feldspar, grossular, diopside and monticellite, and sodalite—have no ^{26}Mg excesses whatsoever even (in the case of one sodalite) at $^{27}Al/^{24}Mg$ as high as 418 (Table 3; Fig. 8b). Kennedy et al. (1997) also analyzed one grossular grain in CAI 3655A and found no ^{26}Mg-excess. A regression through our results for the secondary phases yields a line corresponding to $(^{27}Al/^{26}Al)_0 = (0.16 \pm 1.9) \times 10^{-6}$, but with poor probability of fit (0.09, MSWD = 1.6). The slope and 2σ uncertainty for this regression indicates a minimum formation interval of 3.1 Myr between primary and secondary phases.

Type B2 CAI 4022-1

The only primary phase we analyzed in this CAI is anorthite (Table 3). All analyses except for one show ^{26}Mg excesses, but the results do not show a good correlation between Al/Mg and $^{26}Mg/^{24}Mg$ (Fig. 8c). Many anorthite analyses with relatively high Al/Mg have ^{26}Mg excesses that correspond to less than canonical values of initial $^{26}Al/^{27}Al$ (Fig. 8c). These results can be explained as a result of partial resetting of Mg isotopes during a late-stage thermal event as a consequence of diffusion between anorthite and a phase with lower Al/Mg, such as melilite (e.g., Podosek et al. 1991). In this alteration model, diffusion causes an increase in Al/Mg and a decrease in $^{26}Mg/^{24}Mg$ in anorthite. Our anorthite analysis with the highest Al/Mg has $^{26}Mg/^{24}Mg$ within error of the purported original whole-rock $^{26}Mg/^{24}Mg$ of the CAI (Fig. 8c). If this anorthite equilibrated initially with canonical $^{26}Al/^{27}Al$, then significant isotopic resetting must have occurred subsequently. This result and the analyses with higher ^{26}Mg excesses from this CAI indicate initial isotopic closure with canonical $^{26}Al/^{27}Al$ followed by widely variable resetting.

Most analyses of secondary minerals from CAI 4022-1 show no resolvable ^{26}Mg excesses, but a significant excess was detected in one grossular analysis (Figs. 8c and 8d). This analysis is of grossular adjacent to secondary anorthite in a vein near the margin of the CAI (Fig. 5b). As noted above, some of the secondary feldspar in 4022-1 is relatively coarse-grained, stoichiometric anorthite. Analyses of these crystals yield high Al/Mg and well-resolved, isotopically normal $^{26}Mg/^{24}Mg$ (Fig. 8c). The two sodalite analyses and one grossular analysis also show no ^{26}Mg excess (Fig. 8d). One of the three grossular analyses actually shows a depletion in ^{26}Mg, though this result is nearly within 2σ of isotopically

Table 3. Al-Mg isotopic results.

Analysis no.	Sputtered material	$^{25}Mg/^{24}Mg_{meas}$	$^{26}Mg/^{24}Mg_{meas}$	$^{27}Al/^{24}Mg$	2σ	$^{26}Mg/^{24}Mg_{cor}$	2σ
B1 CAI 3655A, primary phases							
B1-1-01	Anorthite (CL-bright)	0.13073(41)	0.16348(61)	353	19	0.1545	0.0011
B1-1-02	Anorthite (CL-dull)	0.13155(49)	0.15816(72)	190	10	0.1473	0.0013
B1-1-03	Anorthite (CL-dull)	0.13146(48)	0.15847(65)	214	13	0.1478	0.0012
B1-1-05	Melilite	0.13305(15)	0.15261(29)	1.6	0.1	0.1385	0.0004
B1-1-06	Melilite	0.13266(08)	0.15160(13)	1.7	0.1	0.1383	0.0002
B1-1-06b	Spinel	0.12709(10)	0.14035(16)	2.2	0.1	0.1394	0.0003
B1-1-09	Melilite	0.12954(20)	0.14589(33)	14.3	0.8	0.1395	0.0005
B1-2-1	Anorthite (CL-bright)	0.12721(61)	0.15717(81)	387	23	0.1559	0.0016
B1 CAI 3655A, secondary phases							
B1-1-04	Grossular	0.13164(31)	0.14979(41)	74	7	0.1388	0.0008
B1-1-07	Grossular	0.13075(19)	0.14807(27)	27	3	0.1390	0.0005
B1-1-08	Sodalite	0.13376(09)	0.15537(15)	37	4	0.1397	0.0003
B1-1-11	Sec. feldspar	0.13150(19)	0.15049(35)	19.6	2.0	0.1398	0.0006
B1-1-12	Sec. feldspar	0.13242(40)	0.15226(76)	53.5	5.4	0.1395	0.0012
B1-2-2	Grossular	0.12744(19)	0.14105(21)	21.3	2.1	0.1393	0.0005
B1-2-3	Grossular	0.12907(26)	0.14490(28)	49.1	4.9	0.1395	0.0006
B1-2-4	Sodalite	0.12867(32)	0.14404(37)	417.7	41.8	0.1395	0.0008
B1-2-5	Diopside	0.12809(10)	0.14280(14)	1.5	0.2	0.1396	0.0003
B1-2-6	Sec. feldspar	0.12911(30)	0.14489(34)	25.8	2.6	0.1394	0.0007
B1-2-7	Sec. feldspar	0.12784(19)	0.14247(24)	16.8	1.7	0.1398	0.0005
B1-2-8	Monticellite	0.12725(11)	0.14065(12)	0.1	0.0	0.1393	0.0003
B2 CAI 4022-1, primary phases							
B2-1	Anorthite	0.12678(92)	0.14048(92)	1046	49	0.1401	0.0022
B2-3	Anorthite	0.12681(46)	0.14445(53)	345	17	0.1441	0.0011
B2-4a	Anorthite	0.12631(50)	0.15063(61)	340	16	0.1513	0.0013
B2-4j	Anorthite	0.12741(42)	0.15061(50)	422	19	0.1530	0.0014
B2-4m	Anorthite	0.12698(37)	0.14895(55)	572	26	0.1551	0.0015
B2-4b	Anorthite	0.12715(41)	0.14961(49)	238	11	0.1489	0.0010
B2-4c	Anorthite	0.12658(32)	0.14665(43)	223	10	0.1482	0.0010
B2-4d	Anorthite	0.12770(41)	0.15069(56)	208	9	0.1485	0.0010
B2-4e	Anorthite	0.12757(41)	0.15291(55)	156	7	0.1468	0.0008
B2-4f	Anorthite	0.12776(67)	0.15397(83)	251	12	0.1483	0.0011
B2-4g	Anorthite	0.12751(54)	0.15223(80)	231	10	0.1508	0.0011
B2-4h	Anorthite	0.12802(56)	0.15601(73)	608	28	0.1515	0.0017
B2-4i	Anorthite	0.12728(59)	0.15651(82)	441	20	0.1503	0.0014
B2-10b	Anorthite	0.12515(56)	0.14569(71)	477	26	0.1489	0.0014
B2-10c	Anorthite	0.12769(45)	0.15331(57)	298	14	0.1510	0.0011
B2-10d	Anorthite	0.12782(49)	0.15441(57)	329	15	0.1518	0.0012
B2-10g	Anorthite	0.12742(52)	0.14818(66)	413	20	0.1464	0.0013
B2-11a	Anorthite	0.12768(47)	0.15280(66)	376	19	0.1505	0.0012
B2-11b	Anorthite	0.12738(37)	0.15097(44)	235	11	0.1493	0.0009
B2-11c	Anorthite	0.12682(35)	0.15051(44)	243	11	0.1501	0.0009
B2-11d	Anorthite	0.12708(39)	0.14778(47)	257	12	0.1468	0.0010
B2 CAI 4022-1, secondary phases							
B2-5	Grossular	0.12772(19)	0.14107(48)	29.4	2.9	0.1387	0.0005
B2-6	Sec. feldspar	0.12788(60)	0.14186(75)	512	51	0.1391	0.0015
B2-7	Sodalite	0.12692(21)	0.13977(34)	22.5	2.2	0.1391	0.0006
B2-8	Grossular	0.12854(13)	0.14347(17)	12.3	1.2	0.1393	0.0003
B2-9	Grossular	0.12591(12)	0.13867(16)	29.6	2.9	0.1403	0.0003
B2-12	Sec. feldspar	0.12609(25)	0.13831(35)	211	19	0.1396	0.0007
B2-14	Sodalite	0.12582(20)	0.13790(27)	36	3.6	0.1397	0.0005

Table 3. *Continued.* Al-Mg isotopic results.

Analysis no.	Sputtered material	$^{25}Mg/^{24}Mg_{meas}$	$^{26}Mg/^{24}Mg_{meas}$	$^{27}Al/^{24}Mg$	2σ	$^{26}Mg/^{24}Mg_{cor}$	2σ
CTA CAI 3898-2, primary phases							
CTA1-07	Melilite	0.13173(19)	0.15106(34)	34.4	1.8	0.1398	0.0005
CTA1-08	Hibonite	0.12912(16)	0.14521(25)	13.6	0.7	0.1397	0.0004
CTA1-09	Hibonite	0.12828(16)	0.14346(22)	14.0	0.7	0.1398	0.0004
CTA1-10	Spinel	0.12758(11)	0.14138(17)	2.3	0.1	0.1393	0.0003
CTA1-16	Spinel	0.12777(11)	0.14168(17)	2.4	0.1	0.1392	0.0003
CTA1-18	Melilite	0.13016(34)	0.14697(51)	23.3	1.3	0.1392	0.0009
CTA1-21	Melilite	0.13044(14)	0.14737(22)	8.0	0.4	0.1390	0.0004
CTA2-1	Spinel	0.12693(11)	0.14020(16)	2.4	0.1	0.1395	0.0003
CTA2-3	Spinel	0.12643(08)	0.13895(07)	2.3	0.1	0.1394	0.0002
CTA2-6	Melilite	0.12595(82)	0.14017(93)	41.8	2.3	0.1417	0.0020
CTA2-9	Spinel	0.12759(08)	0.14149(10)	2.2	0.1	0.1394	0.0002
CTA CAI 3898-2, secondary phases							
CTA1-01	Sec. feldspar	0.12917(28)	0.14490(44)	25.6	2.6	0.1393	0.0008
CTA1-03	Sec. feldspar (75%), sodalite (25%)	0.13127(18)	0.14935(32)	12.9	1.3	0.1392	0.0005
CTA1-04	Sec. feldspar	0.1296617)	0.14570(31)	11.9	1.2	0.1390	0.0005
CTA1-05	Sec. feldspar	0.13014(24)	0.14729(43)	19.5	2.0	0.1396	0.0007
CTA1-06	Sec. feldspar	0.13224(26)	0.15114(47)	9.9	1.0	0.1388	0.0007
CTA1-11	Grossular	0.12516(28)	0.13868(30)	46.1	4.6	0.1419	0.0007
CTA1-12	Nepheline	0.13014(23)	0.14785(26)	63.8	6.4	0.1401	0.0006
CTA1-13	Sec. feldspar	0.13103(15)	0.15002(26)	23.2	2.3	0.1403	0.0004
CTA1-14	Sec. feldspar	0.13020(22)	0.14772(32)	46.9	4.7	0.1399	0.0006
CTA1-15	Sec. feldspar	0.12794(12)	0.14268(16)	15.9	1.6	0.1398	0.0003
CTA1-19A	Grossular	0.12604(28)	0.13948(45)	37.2	3.7	0.1408	0.0008
CTA1-19B	Nepheline	0.13048(25)	0.14874(29)	132	13	0.1403	0.0006
CTA1-20	Grossular	0.13286(15)	0.15375(23)	12.7	1.3	0.1400	0.0004
CTA2-2	Nepheline	0.12983(32)	0.14659(34)	269	27	0.1396	0.0008
CTA2-4	Sec. feldspar	0.12555(57)	0.13700(64)	88.0	8.8	0.1394	0.0014
CTA2-5	Grossular	0.12800(18)	0.14294(23)	12.0	1.2	0.1399	0.0005
CTA2-7	Grossular	0.12853(08)	0.14376(12)	12.5	1.3	0.1396	0.0002
CTA2-8	Grossular	0.13034(06)	0.14778(08)	12.0	1.2	0.1396	0.0001
FTA CAI 3529-47-1, primary phases							
FTA-2a	Melilite	0.12587(11)	0.13808(15)	9.1	0.5	0.1397	0.0003
FTA-2b	Melilite	0.12614(23)	0.14010(29)	43.0	2.1	0.1412	0.0006
FTA-2c	Melilite	0.12852(18)	0.14416(24)	22.7	1.2	0.1400	0.0005
FTA-7	Melilite	0.12560(29)	0.13861(33)	32.3	1.8	0.1409	0.0007
FTA CAI 3529-47-1, secondary phases							
FTA-1a	Sec. feldspar	0.1263(13)	0.1410(15)	247	25	0.1417	0.0032
FTA-1b	Sec. feldspar	0.13174(15)	0.15002(22)	31.8	3.2	0.1388	0.0004
FTA-3	Sec. feldspar	0.12502(16)	0.13636(24)	22.9	2.3	0.1399	0.0004
FTA-4	Sodalite	0.1276(12)	0.1414(17)	2210	220	0.1394	0.0031
FTA-5	Sec. feldspar	0.12615(36)	0.13996(43)	258	26	0.1410	0.0009
FTA-6	Grossular	0.12834(24)	0.14395(30)	92.2	9.2	0.1401	0.0006
FTA-8b	Sec. feldspar	0.12511(17)	0.13678(25)	22.6	2.3	0.1401	0.0005
FTA-9a	Nepheline	0.12832(13)	0.14347(17)	19.0	1.9	0.1397	0.0003
FTA-10	Sec. feldspar	0.12635(15)	0.13957(20)	25.4	2.5	0.1402	0.0004
FTA-11a	Nepheline	0.12735(24)	0.14137(38)	45.1	4.5	0.1398	0.0007
FTA-11b	Nepheline	0.12622(25)	0.13938(29)	125	13	0.1402	0.0006
FTA-12	Grossular	0.12508(37)	0.13705(47)	156	16	0.1406	0.0009
FTA-13	Nepheline	0.12476(30)	0.13673(34)	72.9	7.3	0.1408	0.0007
FTA-14	Sec. feldspar	0.12625(25)	0.13918(31)	45.3	4.5	0.1400	0.0006
FTA-15	Sec. feldspar	0.12714(35)	0.14109(54)	63.5	6.3	0.1400	0.0009
FTA-16	Sec. feldspar	0.12612(30)	0.13971(37)	119	12	0.1408	0.0008

Note: Because of the fine grain size and intergrown textures, most analyses of secondary minerals include some material sputtered from adjacent grains.
Abbreviations: "meas" and "cor" subscripts of Mg isotopic data indicate measured values and values corrected for mass fractionation. 2σ errors shown in parentheses. Sec. feldspar = secondary feldspar.

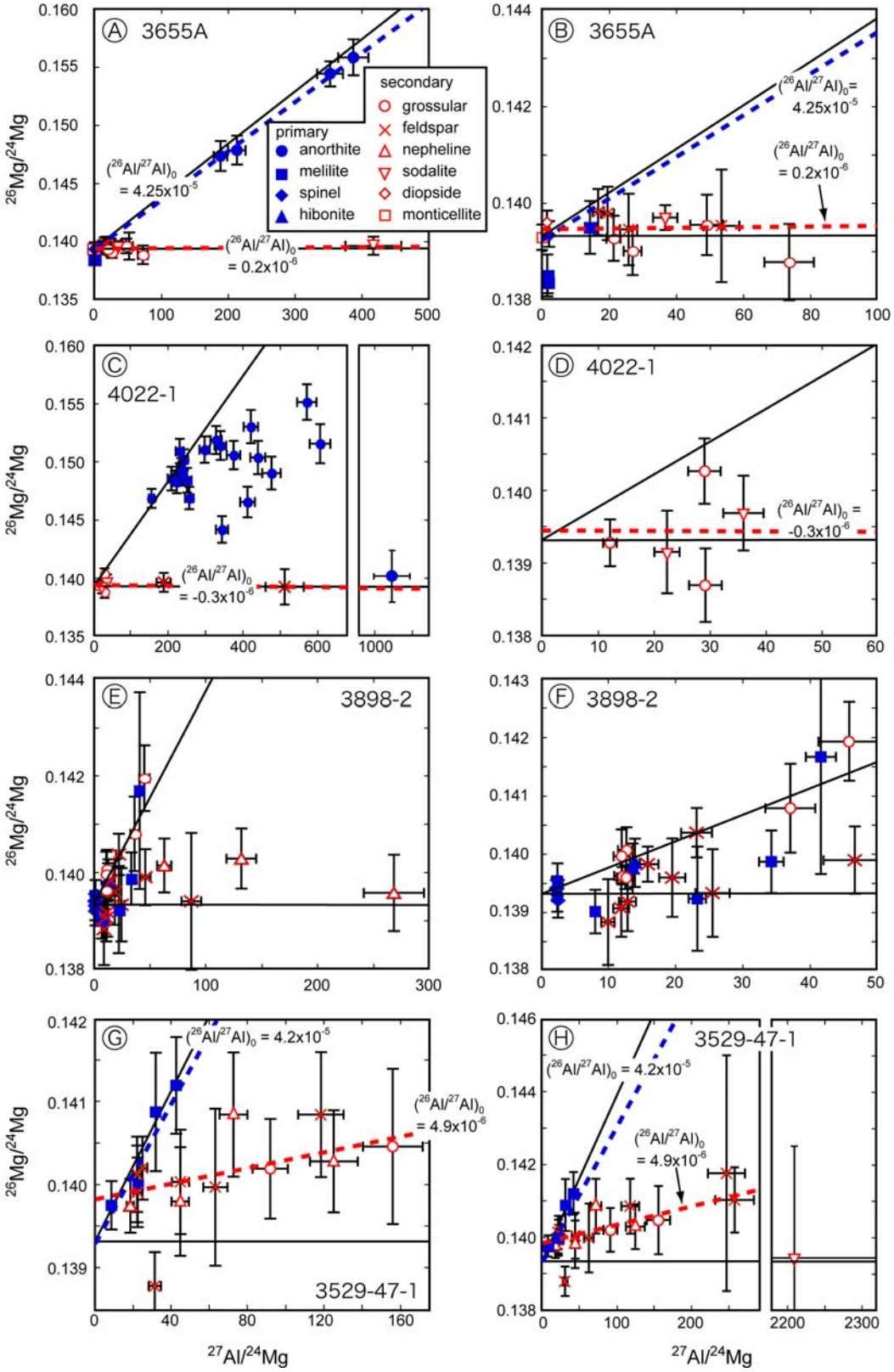

Fig. 8. Al-Mg isotopic results from four Allende CAIs. Error bars show ±2σ. Solid lines are reference lines showing initial $^{26}Al/^{27}Al = 4.5 \times 10^{-5}$ and 0. Dashed lines are fits to data from primary (blue) and secondary (red) minerals. Points used to calculate regressions and uncertainties of the fits are discussed in the text. a, b) Type B1 CAI 3655A. c, d) Type B2 CAI 4022-1. e, f) Compact type A CAI 3898-2. g, h) Fluffy type A CAI 3529-47-1.

normal Mg. This result could represent a true Mg isotope anomaly or an unknown analytical artifact. A regression through all of the secondary minerals except grossular yields a slope corresponding to initial $^{26}Al/^{27}Al = (-0.3 \pm 2.9) \times 10^{-6}$, initial $^{26}Mg/^{24}Mg = 0.13945$ (±0.00040), with a probability of fit = 0.35 and MSWD = 1.05. This regression suggests that sodalite and secondary feldspar in this CAI crystallized or remained open to Mg-diffusion a minimum of 3 Myr after canonical $^{26}Al/^{27}Al$ values (4.5×10^{-9}) were attained.

Compact Type A CAI 3898-2

Al-Mg results from melilite and hibonite in this inclusion mostly show excesses of ^{26}Mg but do not define a simple linear increase with Al/Mg (Table 3; Figs. 8e and 8f); two of the four melilite analyses have no resolvable ^{26}Mg excesses. These results differ from those of Podosek et al. (1991), who reported a well-defined correlation corresponding to an initial ratio of $^{26}Al/^{27}Al = 4.5 \times 10^{-5}$ based on their analyses of melilite, hibonite, pyroxene, and spinel. We note, however, that our error bars are larger than theirs (due to shorter analytical times), and many of our melilite analyses were taken close to altered domains (melilite is prone to isotopic resetting). Our melilite analysis with the highest Al/Mg as well as both of our hibonite analyses fall within error of the regression line of Podosek et al. (1991).

In contrast to the type B CAIs, several analyses of secondary phases in 3898-2 show well-resolved $^{26}Mg/^{24}Mg$ excesses. All of the grossular analyses show $^{26}Mg/^{24}Mg$ excesses. Two grains from a grossular-rich vein yield minor, but resolved, excesses of ^{26}Mg (CTA2-7, CTA 2-8) (Table 3); the other four grossular analyses are from the margins or interiors of feldspathoid-bearing alteration patches, and show well-resolved excesses along a line with slope indicating $(^{26}Al/^{27}Al)_0 = 4.5 \times 10^{-5}$ (Fig. 8f). Two of these analyses have relatively high Al/Mg (CTA1-11 and CTA1-19A) and are from a single alteration patch (Figs. 6c and 6d). Three analyses of secondary feldspar were also collected from this patch; of these, two (CTA1-13 and CTA1-15) have ^{26}Mg excesses consistent with $(^{26}Al/^{27}Al)_0 = 4.5 \times 10^{-5}$, and one (CTA1-14) is approximately within 2σ of normal $^{26}Mg/^{24}Mg$ (Fig. 8f). The two nepheline analyses from this alteration patch have Al/Mg between 50 and 150 and have small resolved excesses of ^{26}Mg (Fig. 8e). The remainder of nepheline and feldspar analyses, from other parts of the CAI, have no resolvable excess $^{26}Mg/^{24}Mg$.

Fluffy Type A CAI 3529-47-1

The only primary phase analyzed in this CAI is melilite, which shows ^{26}Mg excesses correlating with Al/Mg (Table 3). All four analyses are consistent with $(^{26}Al/^{27}Al)_0 = 4.5 \times 10^{-5}$ (Fig. 8g), though a regression yields a slightly lower slope, $(^{26}Al/^{27}Al)_0 = (4.2 \pm 1.7) \times 10^{-5}$, with initial $^{26}Mg/^{24}Mg = 0.13945$ (±0.00040), probability of fit = 0.41 and MSWD = 0.88.

Most of the secondary phases also have ^{26}Mg excesses (Figs. 8g and 8h). The two exceptions are a secondary feldspar with an apparent ^{26}Mg-depletion (FTA-1B) and a single sodalite analysis (FTA-4) with $^{27}Al/^{24}Mg \sim 2200$. We have no petrologic basis for ruling out either of these analyses, yet they clearly deviate from the trend of most results from secondary phases in 3529-47-1 (Figs. 8g and 8h). A regression through all analyses of the secondary phases, except for the two analyses noted above, yields a line corresponding to $(^{26}Al/^{27}Al)_0 = (4.9 \pm 2.8) \times 10^{-6}$, initial $^{26}Mg/^{24}Mg = 0.13984$ (±0.00021), probability of fit = 0.68 and MSWD = 0.77. Using a simple regression to force the $^{26}Mg/^{24}Mg$ intercept through 0.13932 yields a higher slope (9×10^{-6}) but a poor fit ($r^2 = 0.38$). In any case, results from this CAI suggest that most of the secondary phases formed while ^{26}Al was still present, though in concentrations much lower than canonical.

DISCUSSION

Alteration Textures and Mineral Assemblages: Similarities and Differences

Each CAI is characterized by an outer (near-rim) alteration domain composed of feldspathoids, FeO-bearing spinel, lath-like secondary feldspar, and grossular. These feldspathoid-bearing alteration patches exhibit a common textural sequence, with grossular immediately in contact with melilite, secondary feldspar overlying the grossular, and feldspathoids ± grossular overlying the feldspar. In the cases of the three compact CAIs, these alteration domains mantle the entire CAIs just interior to the Wark-Lovering rims; on the fluffy type A CAI, they mantle each individual nodule of the CAI below the individual rim sequences. Melilite was the dominant primary mineral consumed to form these secondary minerals; FeO-bearing spinel presumably replaces primary Mg-rich spinel.

The feldspathoid-bearing alteration in the compact type A CAIs is more abundant than in the type B CAIs, and in the nodules of the fluffy type A CAI over 50% by volume of the melilite has been replaced by the feldspathoid-bearing alteration assemblage (Figs. 1d and 2d). The type B2 CAI, 4022-1, differs from the other three CAIs in having feldspathoid-bearing alteration patches in its interior. Secondary feldspar in these domains is coarser-grained, more equant, and purer anorthite relative to the lath-textured feldspar that occurs along the rim of CAI 4022-1. The only other observed occurrence of this relatively coarse secondary feldspar was in 3898-1, where it was rare.

Grossular-rich veins and patches occur in the interiors of all the CAIs. These grossular-rich domains are concentrated along melilite grain boundaries and apparently formed by replacement of melilite and, to a lesser extent, primary anorthite. As is the case for the feldspathoid-bearing

alteration assemblages, the grossular-rich alteration domains show variations among the CAIs. The two type B CAIs have abundant grossular + monticellite veins, but whereas veins in 4022-1 (type B2) cut primary anorthite, those in 3655A are mostly situated along melilite grain boundaries. Extensive pseudomorphic replacement of melilite by grossular and monticellite, ± wollastonite, occurs in the core of B1 CAI 3655A, where åkermanite content is high ($Åk_{65}$); no comparable textures were identified in the type B2 or the type A CAIs.

Grossular-rich alteration domains are not as abundant in the type A CAIs as in the type Bs. In fact, true grossular-rich veins were not observed at all in fluffy type A CAI 3529-47-1. Rather, more equant masses of grossular protrude into melilite in some nodules (Fig. 7b). Veins are present in compact type A CAI 3898-2, but they are thinner and finer grained than the veins in the type B CAIs. No monticellite or wollastonite was identified in either type A CAI, in contrast to the type B CAIs.

Our observations suggest a general correlation between Åk content and extent of replacement of melilite by the grossular-rich domains. The most extensively replaced melilite has Åk contents near $Åk_{65–72}$ in the core of CAI 3655A, whereas the more gehlenitic melilite in the CAI mantle shows less replacement by the grossular-rich assemblage. Grossular-bearing veins are more abundant in both of the type B CAIs, where melilite compositions of $Åk_{>40}$ are common, than in the type A CAIs, in which most melilite has $Åk_{<40}$. Thus the locations of grossular-rich replacement domains may be controlled by melilite composition, analogous to replacement of zoned plagioclase in some terrestrial rocks. This replacement likely occurred during the open system chemical changes that must have occurred during alteration (Davis and Simon 1994). Independently, however, some grossular-rich alteration may form via a closed system reaction between bordering melilite and primary anorthite, as suggested by Hutcheon and Newton (1981):

$$3\ Ca_2MgSi_2O_7 + Ca_2Al_2SiO_7 + CaAl_2Si_2O_8 = 2\ Ca_3Al_2Si_3O_{12} + 3\ CaMgSiO_4 \quad (1)$$

This reaction cannot, however, explain all of the grossular occurrences in CAIs. First, the accompanying monticellite is characteristic of alteration in the type B CAIs whereas it is absent, or extremely rare, in the type A CAIs; it can hardly be coincidental that a chief primary difference between type B and type A CAIs is the presence of primary anorthite in the former; it is absent from type As. Finally, the extent of pseudomorphic replacement of melilite is greatest in the core of CAI 3655A, where primary anorthite is concentrated. Collectively, our observations indicate that grossular in CAIs formed in two ways: by open system alteration of melilite (especially in type As), and (exclusively in type Bs) by closed-system reaction of melilite with primary anorthite as suggested by Hutcheon and Newton (1981).

In summary, two main types of alteration mineral assemblages in the CAIs can be identified based on mineralogy, composition and texture: (1) feldspathoid-bearing alteration domains formed by replacement of melilite near the Wark-Lovering rims of all four CAIs, and (2) grossular-rich alteration domains in the CAI interiors. Grossular-rich alteration is much more abundant in the type B CAIs than in the type As. The feldspathoid-bearing alteration domains, and at least some of the grossular-rich domains, required an influx of alkalies, halogens, oxidized iron, and probably silica as well to react with primary åkermanite-rich melilite (Grossman and Granapathy 1975; Wark 1981; MacPherson et al. 2005). Some grossular-rich domains in type B CAIs probably formed by closed-system reactions between melilite and primary anorthite (Hutcheon and Newton 1981).

Similar enrichments in alkalies, halides, and FeO have been observed in Allende chondrules and amoeboid olivine aggregates (AOAs) (Krot et al. 1998; Imai and Yurimoto 2003). In contrast, chondrules, CAIs and AOAs in the reduced CV3 chondrites apparently formed by the same primary processes as those in Allende, yet rarely exhibit alkali-FeO alteration to the same extent as the Allende objects (Sylvester et al. 1993; Krot et al. 1998, 2004; Komatsu et al. 2001). The abundance of this type of alteration in Allende, compared with its paucity in the reduced CV3 chondrites has been used as evidence that the alkali-FeO alteration took place on the Allende parent body (Krot et al. 1998, 2000; see review by Brearley 2003) and that the differences between oxidized versus reduced CV3s is a reflection of differing porosity at the time of alteration (MacPherson and Krot 2002).

Al-Mg Isotopes and the Timing and Setting of Alteration

Recognition of Early-Stage and Late-Stage Alteration Event(s)

The most significant results from this study are the finding of well-resolved ^{26}Mg excesses in secondary phases of several of the CAIs, especially the type As. Although sporadic reports of such excesses have been reported previously (e.g., Huss et al. 2001), rarely have systematic excesses been demonstrated. Beyond the important implication for the early formation of some secondary minerals, our results demonstrate that heating on the Allende parent body was not strong enough to completely erase the Mg isotope signatures in these fine-grained secondary minerals.

The strongest indication of an early alteration event comes from compact type A CAI 3898-2, where grossular exhibits consistent excesses of ^{26}Mg correlating with Al/Mg. Four of the six grossular analyses come from a common textural setting—in contact with feldspathoid-bearing alteration patches—and are consistent with $(^{26}Al/^{27}Al)_0 \sim 4.5 \times 10^{-5}$. In one alteration patch, two of three secondary

feldspar analyses also fall along the same line; the third feldspar is marginally resolved from normal Mg; and two nepheline analyses from this patch show small excesses of $^{26}Mg/^{24}Mg$. We interpret these results as a consequence of an early stage of alteration in the nebular setting, best preserved in grossular, followed by variable resetting during later thermal events. Redistribution of isotopes by diffusion between primary and secondary minerals (Podosek et al. 1991) does not account for the correlation between $^{26}Mg/^{24}Mg$ and Al/Mg observed in grossular, and is a less effective mechanism in the absence of primary minerals with high Al/Mg, such as primary anorthite. We see suggestions of similar high $(^{26}Al/^{27}Al)_0$ elsewhere in our data set (e.g., one grossular analysis from a vein near the margin of the type B2 CAI, 4022-1), but there is not such a clear correlation of ^{26}Mg excesses with Al/Mg (Fig. 8d). Based on the results from primary anorthite (Fig. 8c), redistribution of Mg isotopes by diffusion clearly occurred in this CAI and may have played a role in the ^{26}Mg excess detected in this grossular (see Podosek et al. 1991). High inferred $(^{26}Al/^{27}Al)_0$ ratios in secondary minerals also were reported by Huss et al. (2001) in sodalite in a type A inclusion from the ordinary chondrite Semarkona, and in feldspathoids from an Allende fine-grained spinel-rich inclusion (Brigham et al. 1986).

Our study and that of Ushikubo et al. (2006) differ from the other previous work in showing diverse isotopic signatures within neighboring secondary minerals in each CAI, suggesting either differential isotopic resetting during later thermal events or else multiple episodes of secondary alteration. In CAI 3898-2, nepheline in the same region as the grossular with correlated ^{26}Mg excesses has much smaller or no ^{26}Mg excesses. In CAI 4022-1, grossular with clear excess ^{26}Mg is adjacent to secondary anorthite having no excess ^{26}Mg (Fig. 5b). Ushikubo et al. (2006) identified ^{26}Mg excesses in a grossular-bearing domain and no excess ^{26}Mg (i.e., isotopically normal Mg) in a feldspathoid-bearing domain within the single CAI they studied. However, neither the data of Ushikubo et al. (2006) nor our subset of data from CAI 3898-2 permit discriminating between a model in which the secondary minerals with significant ^{26}Mg excesses have different formation ages than those without ^{26}Mg excesses or, alternatively, attributing the differences to incomplete isotopic resetting during later thermal events. The strongest evidence for multiple alteration events is recorded in the isotopic systematics in fluffy type A 3529-47-1, where all but two analyses of secondary minerals show excesses of ^{26}Mg correlated with Al/Mg, thus indicating the in situ decay of live ^{26}Al (Figs. 8g and 8h). Taken at face value, the regression through these points indicates formation (or, at least, closure to diffusion) at $(^{26}Al/^{27}Al)_0 = (4.9 \pm 2.8) \times 10^{-6}$. This result corresponds to a time of 2.3 Myr, with a range of 1.9–3.2 Myr, after formation of not only the primary CAI minerals but also the early generation of secondary minerals noted above (assuming $[^{26}Al/^{27}Al]_0 = 4.5 \times 10^{-5}$). The regression also yields an elevated $^{26}Mg/^{24}Mg$ intercept (0.13984 ± 0.00021) (Figs. 8g and 8h) that is consistent with isotopic resetting during alteration of melilite on the order of 2–3 Myr after its original formation. Given that the melilite in CAI 3529-47-1 has composition $Åk_{10–25}$ with $(^{26}Al/^{27}Al)_0 = 4.2 \times 10^{-5}$ (Fig. 8g), and assuming also that the system is closed on the "whole-rock" scale with regard to Mg and Al (obviously not true for components such as Na and Cl), the calculated $^{26}Mg/^{24}Mg$ after 2.3 Ma is ~0.1402–0.1396. Collectively, the data indicate a recrystallization episode well after primary mineral formation, but they do not discriminate between a parent-body versus a nebular setting of alteration (see below).

Possible Setting for Late-Stage Alteration

All four of the studied CAIs have at least some secondary minerals that show no resolvable ^{26}Mg excess (Table 3; Fig. 8). Most analyses of secondary minerals from the type B CAIs 4022-1 and 3655A have no detectable ^{26}Mg excess (also see Kennedy et al. 1997), as do many analyses from CAI 3898-2, a high Al/Mg sodalite from 3529-47-1 and one primary anorthite from 4022-1. These results indicate that many secondary minerals in each CAI either (a) formed in a setting without much ^{26}Al, or (b) did not close to Al-Mg diffusion until >3 Myr after the canonical Al-Mg signal was acquired by primary minerals, or (c) some combination of (a) and (b). If ^{26}Al was more or less evenly distributed throughout the early solar system, then scenarios (a), (b), and (c) all require some thermal event more than 3 Myr after CAI formation at $(^{26}Al/^{27}Al)_0 \sim 4.5 \times 10^{-5}$.

The fact that all of the CAIs have similar alteration assemblages with similar lack of ^{26}Mg excesses suggests a common setting for this last phase of alteration, but the setting itself has been the subject of much debate. For example, Hsu et al. (2006) used ^{36}Cl-^{36}S and ^{26}Al-^{26}Mg data from an Allende chondrule and a CAI to argue for a late-stage alteration event that post-dated chondrule formation but pre-dated assembly of the Allende parent body. On the other hand, Krot et al. (1997) used vein and common alteration textures in Allende matrix and dark inclusions to argue that the main late-stage alteration event took place on the Allende parent body.

Circumstantial evidence indicates that the alteration could have been nebular, but does not constrain it to be so. Specifically, it seems reasonably clear that some nebular thermal events were occurring at about the same time as late stage CAI alteration. Krot et al. (2005) reported $(^{26}Al/^{27}Al)_0 \sim 5 \times 10^{-6}$ and $\sim 1 \times 10^{-6}$ in primary minerals in two Allende type C CAIs that include chondrule fragments as xenoliths, and suggested that these isotopic ratios might represent a time of incomplete remelting when the chondrule fragments were trapped within the CAI melts. Those authors could not, however, rule out the possibility of some isotopic resetting during Allende parent body heating. If the initial Al isotopic ratios for the two type C CAIs represent pre-parent body

ages, then the similar $(^{26}Al/^{27}Al)_0$ ratio obtained from 3529-47-1 would suggest that the 1.9–3.2 Myr alteration event recorded in this CAI could have happened in a nebular setting. The age-range for these secondary phases from 3529-47-1 also overlaps with Al-Mg ages determined for ferromagnesian chondrules from Semarkona ($[^{26}Al/^{27}Al]_0 \sim 7 \times 10^{-6}$; see Kita et al. 2000) and FeO-rich chondrules from the CO3 chondrite Yamato-81020 ($[^{26}Al/^{27}Al]_0 \sim 4 \times 10^{-6}$) (Kunihiro et al. 2004), again suggesting that the main alteration of 3529-47-1 coincided in time with a nebular event (chondrule formation).

It is not the aim of this section to imply that all CV3 CAIs were altered entirely in a nebular setting. Indeed, some intriguing differences between the different CV3 meteorites strongly suggest that oxidized iron and probably some alkalies as well were mobilized in a parent body setting (MacPherson and Krot 2002). Rather, our results lead us to conclude that CAI alteration occurred over a substantial period of time (at least several million years), and that the time period of 2–3 Myr after primary CAI formation may have included both nebular and parent body events.

Future Work

One of the legacies of Ernst Zinner's career has been the technical development of ion microprobe techniques applied toward cosmochemical studies. This study has pushed the limit of our technology owing to the very fine grain size of the phases studied. Continued improvements in spatial and analytical resolution and ion imaging techniques, including of course the newest generation of NanoSIMS instruments, will lead to higher quality analyses of fine-grained minerals like those analyzed herein.

A long-standing unresolved problem is the nature of the environment in which these secondary minerals formed, and the relative roles of kinetics and thermodynamics in controlling the alteration reactions. The tendency for the alteration phases to occur in separate layers around melilite suggests that small-scale gradients in chemical potential play an important role. Certainly, it is clear that at least some of the phases require an influx of additional components (alkalies, oxidized iron) not originally found in the CAIs. The tools for such a physico-chemical analysis exist in the realm of metamorphic petrology (e.g., in studies of skarns), and this is a fertile area for future study.

CONCLUSIONS

Taken together, our Al-Mg isotopic results indicate multiple events in the formation of secondary minerals in Allende CAIs. Inferred initial $^{26}Al/^{27}Al$ ratios approaching 4.5×10^{-5} in secondary phases from CAI 3898-2 (and possibly in one grossular in CAI 4022-1) imply an early stage of alteration of CAIs in the nebular setting. Although most previous analyses of CAI secondary phases indicated a much later (>2–3 Myr) timing for the secondary alteration, we note that Huss et al. (2001) reported that feldspathoid from a CAI in an ordinary chondrite that also yields canonical initial $^{26}Al/^{27}Al$. Thus, early stage alteration of CAIs was not restricted to CV3 chondrites. The observation that such open-system alteration began early enough to overlap with nebular melting events, and was a continuing process, means it is very likely that the evolving bulk compositions of CAIs were affected by multiple episodes of alteration and subsequent remelting as has been proposed previously (MacPherson and Davis 1993; Beckett et al. 2000; Simon et al. 2005).

Most analyses of secondary minerals from fluffy type A CAI 3529-47-1 indicate these minerals formed in the presence of ^{26}Al at an initial abundance ratio of $^{26}Al/^{27}Al \sim 5 \times 10^{-6}$. The alteration of this CAI took place on the order of 2 Myr after the formation of melilite having canonical initial $^{26}Al/^{27}Al$ ($\sim 5 \times 10^{-5}$). This event approximately coincides in time with known nebular events (e.g., chondrule formation) but, given the uncertainties of our results, a parent-body setting remains plausible. The prevalence of elevated initial $^{26}Al/^{27}Al$ in secondary minerals of the type A CAIs supports the idea that type As are less reprocessed than type Bs and thus better preserve evidence for pre-parent body alteration than the latter.

Secondary minerals with no ^{26}Mg excesses were identified in all four of the CAIs investigated in this study. All but two of the secondary minerals analyzed in the type B CAIs yielded no resolvable ^{26}Mg excesses, suggesting formation in the absence of ^{26}Al. These results suggest a stage of alteration in the absence of ^{26}Al, at least 3 Myr after the formation of CAIs, possibly but not necessarily on the Allende parent body. Iodine-xenon results are consistent with a time gap exceeding 3 Myr between CAI formation and alteration on the Allende parent body (Swindle et al. 1983, 1988; Swindle 1998). However, parent-body alteration was not pervasive enough to reset isotopic systems in secondary minerals in all CAIs.

Acknowledgments–We take great pleasure in dedicating this paper to Ernst Zinner, a pioneer in the field of SIMS, an inspiration, and a treasured friend. We look forward to toasting (top-shelf cognac, of course!) his health for many more years. This work was supported by NASA grants NNG04GK47G and NAG5-10468 (both to G. J. M.), NNG05GH37G (Y. G.); Monbu-kagaku-sho Grant-in-Aid of Scientific Research no. 18540483 (T. J. F.); and travel funds from Waseda University. We thank G. Huss and T. Ushikubo for discussions and assistance with ion microprobe analyses. We thank Amelia Logan, Scott Whittaker, and A. Yonemochi for assistance with SEM imaging and electron microprobe analyses. The four CAIs investigated in detail in this study were selected from a larger group of CAIs that had previously been documented by Dr. G. L. Kim. Constructive reviews by Drs. Weibiao Hsu and Justin Simon greatly improved the manuscript.

Editorial Handling—Dr. Larry Nittler

REFERENCES

Beckett J. R., Simon S. B., and Stolper E. 2000. The partitioning of Na between melilite and liquid: Part II. Applications to type B inclusions from carbonaceous chondrites. *Geochimica et Cosmochimica Acta* 64:2519–2534.

Brearley A. J. 2003. Nebular versus parent-body processing. In *Meteorites, comets, and planets*, edited by Davis A. M. Treatise on Geochemistry, vol. 1. Oxford: Elsevier-Pergamon. pp. 247–268.

Brigham C. A., Hutcheon I. D., Papanastassiou D. A., and Wasserburg G. J. 1986. Evidence for ^{26}Al and Mg isotopic heterogeneity in a fine-grained CAI (abstract). 17th Lunar and Planetary Science Conference. pp. 85–86.

Catanzaro E. J., Murphy T. J., Garner E. L., and Shields W. R. 1966. Absolute isotopic abundance ratios and atomic weight of magnesium. *Journal of Research of the National Bureau of Standards* 70A:453–458.

Christophe Michel-Levy M. 1986. Etude comparative des chondrite carbonees d'Allende et de Leoville I. Mineralogy, petrography, chimie. *Bulletin du Museum National d'Histoire Naturelle*. 4e serie. Section C 8:89–147.

Cosarinsky M., Taylor D. J., and McKeegan K. D. 2006. Aluminum-26 model ages of hibonite and spinel from type A inclusions in CV chondrites (abstract #2357). 32nd Lunar and Planetary Science Conference. CD-ROM.

Cuzzi J. N. and Zahnle K. J. 2004. Material enhancement in protoplanetary nebulae by particle drift through evaporation fronts. *The Astrophysical Journal* 614:490–496.

Cuzzi J. N., Ciesla F. J., Petaev M. I., Krot A. N., Scott E. R. D., and Weidenschilling S. J. 2005. Nebula evolution of thermally processed solids: Reconciling models and meteorites. In *Chondrites and the protoplanetary disk*, edited by Krot A. N., Scott E. R. D., and Reipurth B. San Francisco: Astronomical Society of the Pacific. pp. 732–773.

Davis A. M., Simon S. B., and Grossman L. 1994. Alteration of Allende type B1 CAIs: When, where and how (abstract). 25th Lunar and Planetary Science Conference. pp. 315–316.

Ebel D. S. and Grossman L. 2000. Condensation in dust-enriched systems. *Geochimica et Cosmochimica Acta* 64:339–366.

Fahey A. J., Zinner E. K., Crozaz G., and Kornacki A. S. 1987. Microdistributions of Mg isotopes and REE abundances in a type A calcium-aluminum-rich inclusion from Efremovka. *Geochimica et Cosmochimica Acta* 51:3215–3229.

Gray C. M. and Papanastassiou D. A. 1973. The identification of early condensates from the solar nebula. *Icarus* 20:213–239.

Grossman L. 1972. Condensation in the primitive solar nebula. *Geochimica et Cosmochimica Acta* 36:597–619.

Grossman L. 1975. Petrography and mineral chemistry of Ca-rich inclusions in the Allende meteorite. *Geochimica et Cosmochimica Acta* 39:433–454.

Grossman L. 1980. Refractory inclusions in the Allende meteorite. *Annual Reviews of Earth and Planetary Science* 8:559–608.

Grossman L. and Granapathy R. 1975. Volatile elements in Allende inclusions. Proceedings, 6th Lunar Science Conference. pp. 1729–1736.

Hashimoto A. and Grossman L. 1987. Alteration of Al-rich inclusions inside amoeboid olivine aggregates in the Allende meteorite. *Geochimica et Cosmochimica Acta* 51:1685–1704.

Hsu W., Guan Y., Leshin L. A., Ushikubo T., and Wasserburg G. J. 2006. A late episode of irradiation in the early solar system: Evidence from extinct ^{36}Cl and ^{26}Al in meteorites. *The Astrophysical Journal* 640:525–529.

Huss G. R., MacPherson G. J., Wasserburg G. J., Russell S. S., and Srinivasan G. 2001. Aluminum-26 in calcium-aluminum-rich inclusions and chondrules from unequilibrated ordinary chondrites. *Meteoritics & Planetary Science* 36:975–997.

Hutcheon I. D. and Newton R. C. 1981. Mg isotopes, mineralogy and mode of formation of secondary phases in C3 refractory inclusions (abstract). 12th Lunar and Planetary Science Conference. pp. 491–493.

Imai H. and Yurimoto H. 2003. Oxygen isotopic distribution in an amoeboid olivine aggregate from the Allende CV chondrite: Primary and secondary processes. *Geochimica et Cosmochimica Acta* 67:765–772.

Kennedy A. K., Beckett J. R., Edwards D. A., and Hutcheon I. D. 1997. Trace element disequilibria and magnesium isotope heterogeneity in 3655A: Evidence for a complex multi-stage evolution of a typical Allende type B1 CAI. *Geochimica et Cosmochimica Acta* 61:1541–1561.

Kita N. T., Nagahara H., Togashi S., and Morishita Y. 2000. A short duration of chondrule formation in the solar nebula: Evidence from ^{26}Al in Semarkona ferromagnesian chondrules. *Geochimica et Cosmochimica Acta* 64:3913–3922.

Kita N. T., Huss G. R., Tachibana S., Amelin Y., Nyquist L. E., and Hutcheon I. D. 2005. Constraints on the origin of chondrules and CAIs from short-lived and long-lived radionuclides. In *Chondrites and the protoplanetary disk*, edited by Krot A. N., Scott E. R. D., and Reipurth B. San Francisco: Astronomical Society of the Pacific. pp. 558–587.

Komatsu M., Krot A. N., Petaev M. I., Ulyanov A. A., Keil K., and Miyamoto M. 2001. Mineralogy and petrography of amoeboid olivine aggregates from the reduced CV3 chondrites Efremovka, Leoville and Vigarano: Products of nebular condensation and accretion. *Meteoritics & Planetary Science* 36:629–641.

Krot A. N., Scott E. R. D., and Zolensky M. E. 1995. Mineralogical and chemical modification of components in CV3 chondrites: Nebular or asteroidal processing. *Meteoritics* 30:748–776.

Krot A. N., Petaev M. I., Scott E. R. D., Choi B.-G., Zolensky M. E., and Keil K. 1998. Progressive alteration in CV3 chondrites: More evidence for asteroidal alteration. *Meteoritics & Planetary Science* 33:1065–1085.

Krot A. N., Meibom A., and Keil K. 2000. A clast of Bali-like oxidized CV material in the reduced CV chondrite breccia Vigarano. *Meteoritics & Planetary Science* 35:817–825.

Krot A. N., MacPherson G. J., Ulyanov A. A., and Petaev M. I. 2004. Fine-grained, spinel-rich inclusions from the reduced CV chondrite Efremovka: I. Mineralogy, petrology and bulk chemistry. *Meteoritics & Planetary Science* 39:1517–1553.

Krot A. N., Yurimoto H., Hutcheon I. D., and MacPherson G. J. 2005. Chronology of the early solar system from chondrule-bearing calcium-aluminum-rich inclusions. *Nature* 434:998–1001.

Kunihiro T., Rubin A. E., McKeegan K. D., and Wasson J. T. 2004. Initial ^{26}Al/^{27}Al in carbonaceous-chondrite chondrules: Too little ^{26}Al to melt asteroids. *Geochimica et Cosmochimica Acta* 68: 2947–2957.

Lee T., Papanastassiou D. A., and Wasserburg G. J. 1976. Demonstration of ^{26}Mg excess in Allende and evidence for ^{26}Al. *Geophysical Research Letters* 3:41–44.

Lin Y., Guan Y., Leshin L. A., Ouyang Z., and Wang D. 2005. Short-lived chlorine-36 in a Ca- and Al-rich inclusion from the Ningqiang carbonaceous chondrite. *Proceedings of the National Academy of Sciences* 102:1306–1311.

Ludwig K. R. 2003. *Isoplot 3.00: A geochronological toolkit for Microsoft Excel*. Berkeley Geochronology Center Special Publication No. 4. 70 p.

MacPherson G. J. 2003. Calcium-aluminum-rich inclusions in chondritic meteorites. In *Meteorites, comets, and planets*, edited

by Davis A. M. Treatise on Geochemistry, vol. 1. Oxford: Elsevier-Pergamon. pp. 201–246.

MacPherson G. J. and Grossman L. 1984. "Fluffy" type A Ca-, Al-rich inclusions in the Allende meteorite. *Geochimica et Cosmochimica Acta* 48:29–46.

MacPherson G. J. and Davis A. M. 1993. A petrologic and ion microprobe study of a Vigarano type B refractory inclusion: Evolution by multiple stages of alteration and melting. *Geochimica et Cosmochimica Acta* 57:231–243.

MacPherson G. J. and Huss G. R. 2005. Petrogenesis of Al-rich chondrules: Evidence from bulk compositions and phase equilibria. *Geochimica et Cosmochimica Acta* 69:3099–3127.

MacPherson G. J. and Krot A. N. 2002. Distribution of Ca-Fe-silicates in CV3 chondrites: Possible controls by parent-body compaction (abstract). *Meteoritics & Planetary Science* 37:A91.

MacPherson G. J., Davis A. M., and Zinner E. K. 1995. The distribution of aluminum-26 in the early solar system—A reappraisal. *Meteoritics* 30:365–386.

MacPherson G. J., Wark D. A., and Armstrong J. T. 1988. Primitive material surviving in chondrites: Refractory inclusions. In *Meteorites and the early solar system*, edited by Kerridge J. F. and Matthews M. S. Tucson, Arizona: The University of Arizona Press. pp. 746–807.

MacPherson G. J., Huss G. R., and Davis A. M. 2003. Extinct ^{10}Be in type A calcium-aluminum-rich inclusions from CV chondrites. *Geochimica et Cosmochimica Acta* 67:3165–3179.

MacPherson G. J., Simon S. B., Davis A. M., Grossman L., and Krot A. N. 2005. Calcium-aluminum-rich inclusions: Major unanswered questions. In *Chondrites and the protoplanetary disk*, edited by Krot A. N., Scott E. R. D., and Reipurth B. San Francisco: Astronomical Society of the Pacific. pp. 225–250.

McKeegan K. D. and Davis A. M. 2003. Early solar system chronology. In *Meteorites, comets, and planets*, edited by Davis A. M. Treatise on Geochemistry, vol. 1. Oxford: Elsevier-Pergamon. pp. 431–460.

Paque J. 1990. Relict grains in a Ca-Al-rich inclusion from Allende (abstract). 21st Lunar and Planetary Science Conference. pp. 932–933.

Podosek F. A., Zinner E. K., MacPherson G. J., Lundberg L. L., Brannon J. C., and Fahey A. J. 1991. Correlated study of initial ^{87}Sr/^{86}Sr and Al-Mg isotopic systematics and petrologic properties in a suite of refractory inclusions from the Allende meteorite. *Geochimica et Cosmochimica Acta* 55:1083–1110.

Scott E. R. D. and Krot A. N. 2005. Chondritic meteorites and the high-temperature nebular origins of their components. In *Chondrites and the protoplanetary disk*, edited by Krot A. N., Scott E. R. D., and Reipurth B. San Francisco: Astronomical Society of the Pacific. pp. 15–53.

Shu F. H., Shang H., and Lee T. 1996. Toward an astrophysical theory of chondrites. *Science* 271:1545–1552.

Simon S. B., Grossman L., and Davis A. M. 2005. A unique type B inclusion from Allende with evidence for multiple stages of melting. *Meteoritics & Planetary Science* 40:461–475.

Stoll G. and Jochum K. P. 1999. MIC-SSMS analyses of eight new geological standard glasses. *Fresenius Journal of Analytical Chemistry* 364:380–384.

Stolper E. 1982. Crystallization sequences of Ca-Al-rich inclusions from Allende: An experimental study. *Geochimica et Cosmochimica Acta* 46:2159–2180.

Sylvester P. J., Simon S. B., and Grossman L. 1993. Refractory inclusions from the Leoville, Efremovka, and Vigarano C3V chondrites: Major element differences between types A and B, and extraordinary refractory siderophile element compositions. *Geochimica et Cosmochimica Acta* 57:3763–3784.

Swindle T. D. 1998. Implications of iodine-xenon studies for the timing and location of secondary alteration. *Meteoritics & Planetary Science* 33:1147–1155.

Swindle T. D., Caffee M. W., Hohenberg C. M., and Lindstrom M. M. 1983. I-Xe studies of individual Allende chondrules. *Geochimica et Cosmochimica Acta* 47:2157–2177.

Swindle T. D., Caffee M. W., and Hohenberg C. M. 1988. Iodine-xenon studies of Allende inclusions: Eggs and the Pink Angel. *Geochimica et Cosmochimica Acta* 52:2215–2227.

Ushikubo T., Guan Y., Hiyagon H., Sugiura N., and Leshin L. A. 2006. ^{36}Cl, ^{26}Al, and oxygen isotopes in an Allende CAI: Implications for secondary alteration in the early solar system (abstract #2082). 37th Lunar and Planetary Science Conference. CD-ROM.

Wark D. A. 1981. Alteration and metasomatism of Allende Ca-Al-rich materials (abstract). 12th Lunar and Planetary Science Conference. pp. 1145–1147.

Wark D. A. and Lovering J. F. 1977. Marker events in the early solar system: Evidence from rims on Ca-Al-rich inclusions in carbonaceous chondrites. Proceedings, 8th Lunar Science Conference. pp. 95–112.

Wark D. A. and Lovering J. F. 1982a. Evolution of Ca-Al-rich bodies in the earliest solar system: Growth by incorporation. *Geochimica et Cosmochimica Acta* 46:2595–2607.

Wark D. A. and Lovering J. F. 1982b. The nature and origin of type B1 and B2 Ca-Al-rich inclusions in the Allende meteorite. *Geochimica et Cosmochimica Acta* 46:2581–2594.

Yoneda S. and Grossman L. 1995. Condensation of CaO-MgO-Al_2O_3-SiO_2 liquids from cosmic gases. *Geochimica et Cosmochimica Acta* 59:3413–3444.

York D. 1969. Least-squares fitting of a straight line with correlated errors. *Earth and Planetary Science Letters* 5:320–324.

Young E. D. and Galy A. 2004. The isotope geochemistry and cosmochemistry of magnesium. In *Geochemistry of non-traditional stable isotopes*, edited by Johnson C. M., Beard B. L., and Albarede F. Washington, D.C.: Mineralogical Society of America. pp. 197–230.

Young E. D., Simon J. I., Galy A., Russell S. S., Tonui E., and Lovera O. 2005. Supra-canonical ^{26}Al/^{27}Al and the residence time of CAIs in the solar protoplanetary disk. *Science* 308:223–227.